The Astrophysical Journal, 982:16 (21pp), 2025 March 20 https://doi.org/10.3847/1538-4357/adb72b

Unsupervised Machine Learning for Classifying CHIME Fast Radio Bursts and Investigating Empirical Relations

Da-Chun Qiang[1], Jie Zheng[1], Zhi-Qiang You[1], and Sheng Yang[1,2]
[1] Institute for Gravitational Wave Astronomy, Henan Academy of Sciences, Zhengzhou 450046, Henan, People's Republic of China; sheng.yang@hnas.ac.cn
[2] INAF Osservatorio Astronomico di Padova, Vicolo dell'Osservatorio 5, I-35122 Padova, Italy
Received 2024 November 21; revised 2025 February 12; accepted 2025 February 13; published 2025 March 12

Abstract

Fast radio bursts (FRBs) are highly energetic millisecond-duration astrophysical phenomena typically categorized as repeaters or nonrepeaters. However, observational limitations may result in misclassifications, potentially leading to a higher proportion of repeaters than currently identified. In this study, we leverage unsupervised machine learning techniques to classify FRBs using data from the CHIME/FRB catalogs, including both the first catalog and a recent repeater catalog. By employing Uniform Manifold Approximation and Projection for dimensionality reduction and clustering algorithms (k-means and Hierarchical Density-Based Spatial Clustering of Applications with Noise), we successfully segregate repeaters and nonrepeaters into distinct clusters, identifying over 100 potential repeater candidates. Our analysis reveals several empirical relations within the clusters, including the $\log \Delta t_{sc} - \log \Delta t_{rw}$, $\log \Delta t_{sc} - \log T_B$, and r–γ correlations, where Δt_{sc}, Δt_{rw}, T_B, r, and γ represent the scattering time, rest-frame width, brightness temperature, spectral running, and spectral index, respectively. The Chow test results reveal that while some repeaters and nonrepeaters share similar empirical relationships, the overall distinctions between the two groups remain significant, reinforcing the classification of FRBs into repeaters and nonrepeaters. These findings provide new insights into the physical properties and emission mechanisms of FRBs. This study demonstrates the effectiveness of unsupervised learning in classifying FRBs and identifying potential repeaters, paving the way for more precise investigations into their origins and applications in cosmology. Future improvements in observational data and machine learning methodologies are expected to further enhance our understanding of FRBs.

Unified Astronomy Thesaurus concepts: Radio transient sources (2008); Classification (1907); Clustering (1908); Dimensionality reduction (1943)

1. Introduction

Fast radio bursts (FRBs) are highly energetic astronomical phenomena characterized by millisecond-duration emissions. The first FRB signal was discovered in 2007 by D. R. Lorimer et al. (2007), and their existence was firmly established in 2013, when D. Thornton et al. (2013) published observations of four similar events detected by the Australian Parkes Radio Telescope. Since then, FRBs have drawn significant attention in both astronomy and cosmology (e.g., H. Gao et al. 2014; B. Zhang 2014; E. F. Keane 2018; D. R. Lorimer 2018; M.-J. Zhang & H. Li 2018; F. Y. Wang & G. Q. Zhang 2019; D.-C. Qiang & H. Wei 2020, 2021; F. Y. Wang et al. 2020a; W.-Y. Wang et al. 2020b; D. Xiao et al. 2021, 2022; R. C. Zhang et al. 2021; E. Petroff et al. 2022; D. Xiao & Z.-G. Dai 2022; R. C. Zhang & B. Zhang 2022; B. Wang & B. Wang & J.-J. Wei 2023). However, the origin of FRBs remains unknown.

To explore their origin, numerous radio telescopes have dedicated time and efforts to FRBs, such as the Deep Synoptic Array (G. Hallinan et al. 2019; J. Kocz et al. 2019), Arecibo (L. G. Spitler et al. 2014), Parkes (e.g., D. R. Lorimer et al. 2007; S. Burke-Spolaor & K. W. Bannister 2014; V. Ravi & P. D. Lasky 2014; E. Petroff et al. 2015), the Canadian Hydrogen Intensity Mapping Experiment (CHIME; CHIME/FRB Collaboration et al. 2018), the Five-hundred-meter Aperture Spherical Radio Telescope (D. Li & Z. Pan 2016), and the Australian Square Kilometer Array Pathfinder (R. M. Shannon et al. 2024). So far, nearly a thousand FRBs have been observed (E. Petroff et al. 2016; CHIME/FRB Collaboration et al. 2021; F. Jankowski et al. 2023; J. Xu et al. 2023), with nearly 100 of them having known redshifts (e.g., A. C. Gordon et al. 2023; M. Bhardwaj et al. 2024; C. J. Law et al. 2024; K. Sharma et al. 2024). To date, the largest FRB sample is the first CHIME/FRB catalog (CHIME/FRB Collaboration et al. 2021).

Based on observational characteristics, FRBs are broadly classified into two categories, i.e., repeaters and nonrepeaters. As the names suggest, repeaters are sources that have exhibited multiple bursts, whereas nonrepeaters have only been observed to burst once. Since the discovery of the first repeater, FRB 20121102 (L. G. Spitler et al. 2016), more than 50 FRBs have been identified as repeaters to date (P. Kumar et al. 2019; E. Fonseca et al. 2020; CHIME/FRB Collaboration et al. 2021, 2023; F. Kirsten et al. 2022; C. H. Niu et al. 2022; H. Xu et al. 2022), while most of the remaining ones are classified as nonrepeaters. However, V. Ravi (2019) suggests that the volumetric rate of nonrepeating FRBs might exceed that of cataclysmic events and the formation rate of compact objects, implying that the majority of FRBs should be repeaters. Some studies also propose that more than half of the FRBs in the first CHIME/FRB catalog could be repeaters (S. Yamasaki et al. 2023; K. McGregor & D. R. Lorimer 2024). Furthermore, several FRBs initially identified as nonrepeaters were later observed to repeat (CHIME/FRB Collaboration et al. 2023).

These suggest that many of the FRBs currently classified as nonrepeaters might actually be potential repeaters, with only a single burst detected due to various observational factors. As a result, some studies have attempted to identify potential repeaters among apparent nonrepeating FRBs, and one of the methods being employed is machine learning.

Machine learning is an artificial intelligence technique that allows computers to learn from data and make predictions or decisions without being explicitly programmed (T. Cover & P. Hart 1967; D. E. Rumelhart et al. 1986). Machine learning is generally categorized into three types, i.e., supervised learning, unsupervised learning, and semi-supervised learning (e.g., V. Vapnik 1999; L. Breiman 2001; C.-C. Chang & C.-J. Lin 2011; A. P. Dempster et al. 2018). Using algorithms to uncover patterns in the data can be applied to tasks such as classification, regression, clustering, and optimization. Currently, machine learning has already been widely used in the detection and analysis of FRBs (e.g., K. L. Wagstaff et al. 2016; Y. G. Zhang et al. 2018; D. Wu et al. 2019; K. Adámek & W. Armour 2020; D. Agarwal et al. 2020; X. Yang et al. 2021; S. Bhatporia et al. 2023). For instance, within the first CHIME/FRB catalog data set, B. H. Chen et al. (2021) and J.-M. Zhu-Ge et al. (2022) identify 188 and 117 repeater candidates from 474 nonrepeating FRBs via unsupervised learning, respectively. X. Yang et al. (2023) instead discovered 145 repeaters, using FRB morphology as features, while J.-W. Luo et al. (2022) identified dozens of repeater candidates with various supervised learning methods. Furthermore, J.-W. Luo et al. (2022) found that the most prominent factors for distinguishing between nonrepeating and repeating FRBs are the brightness temperature and rest-frame frequency bandwidth, whereas W.-P. Sun et al. (2025) found spectral running may play a role instead. Furthermore, some studies have used machine learning techniques to classify thousands of bursts from highly active repeaters, such as FRB 20121102 (B. J. R. Raquel et al. 2023) and FRB 20201124A (B. H. Chen et al. 2023), in an effort to analyze their potential radiation mechanisms.

In addition to classifying FRBs based on their repeatability, some studies have also investigated the clustering of FRBs using characteristics beyond repeatability, as well as the empirical relationships among these features. For instance, similar to the well-known classification of gamma-ray bursts (GRBs), where short GRBs exhibit short prompt emissions and are mostly associated with the old population, while long GRBs with long prompt emissions are mostly associated with the young population (B. Zhang et al. 2007; P. Kumar & B. Zhang 2014), H.-Y. Guo & H. Wei (2022) proposed classifying FRBs based on their association with either old or young stellar populations. They discovered several tight empirical relations for nonrepeaters in the first CHIME/FRB catalog, such as $\log E - \log L_\nu$, $\log E - \log \mathrm{DM_E}$, and $\log \mathrm{DM_E} - \log L_\nu$, where log means the logarithm to base 10 and E, $\mathrm{DM_E}$, and L_ν are the isotropic energy, the extragalactic dispersion measure (DM), and spectral luminosity, respectively. Similar empirical relations were found for nonrepeaters associated with old populations and all nonrepeaters, though with notably different slopes and intercepts, such as $\log F_\nu - \log S_\nu$, $\log \mathrm{DM_E} - \log S_\nu$, and $\log F_\nu - \log \mathrm{DM_E}$, where F_ν is specific fluence and S_ν is flux. Many empirical relations still hold for localized FRBs (L.-Y. Li et al. 2024). Based on these empirical relations, FRBs could potentially serve as standard candles, allowing cosmological models to be constrained without relying on DM measurements (H.-Y. Guo & H. Wei 2024). X. J. Li et al. (2021) classified FRBs into short ($W < 100$ ms) and long ($W > 100$ ms) bursts, where W represents the pulse width. A strong power-law correlation between fluence and peak flux density was identified for these categories. D. Xiao & Z.-G. Dai (2022) classified repeating FRBs into classical ($T_B \geqslant 10^{33}$ K) and atypical ($T_B < 10^{33}$ K) bursts, where T_B refers to the brightness temperature. A tight power-law correlation between pulse width and fluence was also observed for classical bursts.

CHIME has recently released a new repeater catalog (CHIME/FRB Collaboration et al. 2023), significantly increasing the data available on repeaters. This expanded data set is expected to improve the accuracy of identifying repeater candidates through machine learning. In this paper, we will apply unsupervised learning methods to classify the FRBs from the combined data of these two catalogs into different clusters, find potential repeaters among the nonrepeaters, and analyze possible empirical relations across these clusters. This paper is structured as follows. In Section 2, we present the selected CHIME data and the features used in our analysis. Section 3 introduces two types of unsupervised machine learning methods, i.e., dimensionality reduction and clustering, as well as evaluation metrics. In Section 4, we present the results of the dimensionality reduction and clustering, then we analyze the potential empirical relations. Finally, Section 5 provides our conclusions.

2. Data Set

2.1. Sample Construction

In this paper, we use the largest available FRB data from CHIME to date, including the first CHIME/FRB catalog (Cat1; CHIME/FRB Collaboration et al. 2021) and the CHIME/FRB Collaboration 2023 catalog (Cat2023; CHIME/FRB Collaboration et al. 2023). Cat1 includes 536 events (474 nonrepeaters and 62 repeat bursts from 18 repeaters). There are 600 sub-bursts in total, because of multiple peaks appearing in the light curves of FRBs. Cat2023 contains 127 events from 39 repeaters,[3] or 151 sub-bursts for all events. Since there are six FRBs in Cat1 with flux and fluence values of zero, we excluded those FRBs. Additionally, six nonrepeaters in Cat1, identified as repeaters, are duplicates in Cat2023, resulting in 739 FRB bursts used in this paper.

2.2. Feature Selection

We treat all sub-bursts as individual bursts and use their features for machine learning algorithms. To provide a more comprehensive description of an FRB event, we include a broad range of parameters, based on their usage in previous research, as different studies emphasize different features and identify varying important ones (e.g., B. H. Chen et al. 2022; J.-W. Luo et al. 2022; J.-M. Zhu-Ge et al. 2022; W.-P. Sun et al. 2025). These parameters can be divided into two

[3] In fact, CHIME/FRB Collaboration et al. (2023) marked 14 FRB sources as repeater candidates, due to lower significance, indicating that the burst-to-burst DM and sky-position differences are larger compared to other confirmed repeaters, and their repetition rates are relatively low. In this study, we consider these 14 FRB sources as repeaters, as they warrant further follow-up observations for potential confirmation.

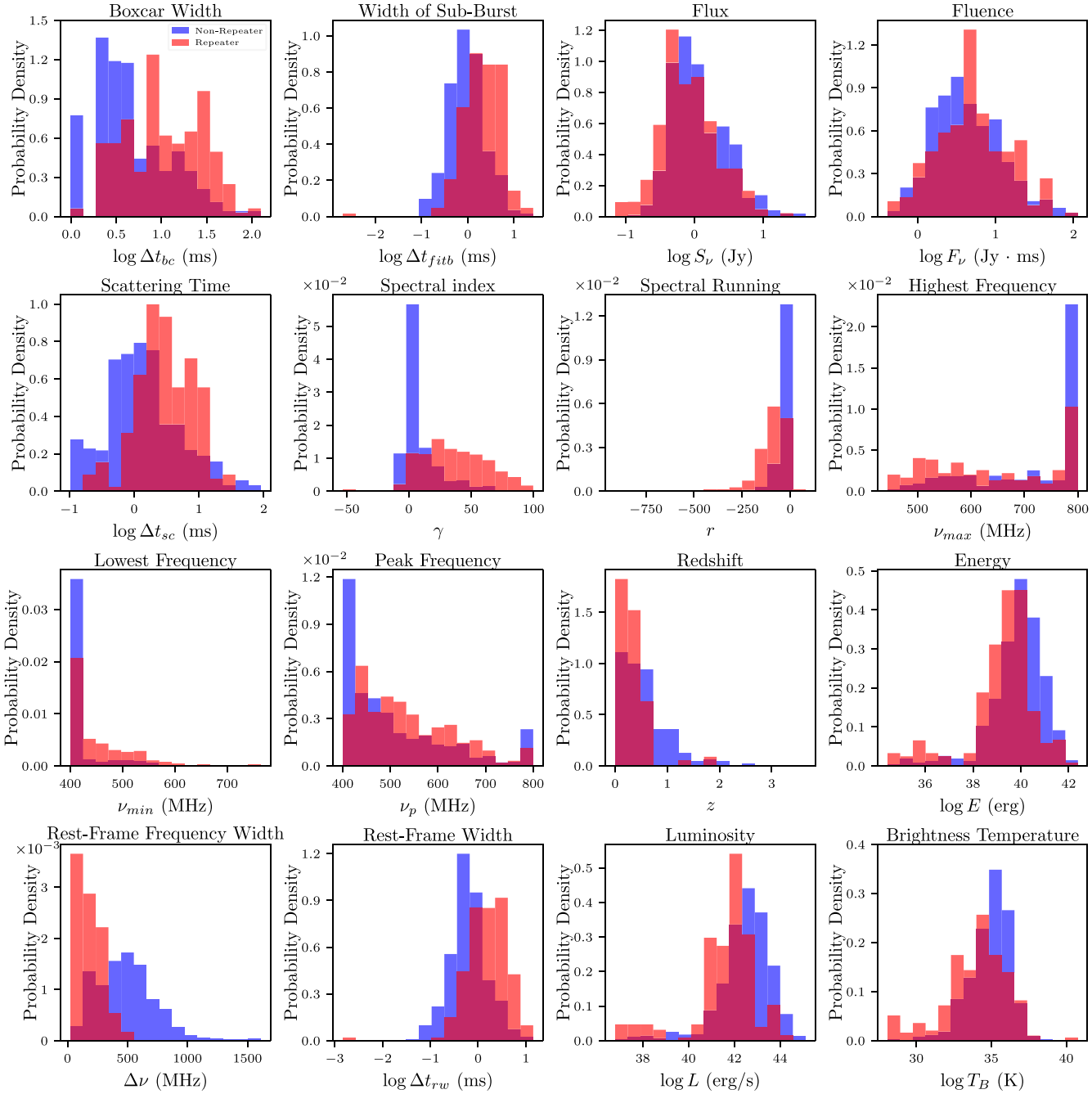

Figure 1. The distributions of observed and derived parameters for nonrepeaters and repeaters are shown separately, forming the input data used for unsupervised learning. For more details, refer to Section 2.

categories—observational parameters (original data provided by Cat1 and Cat2023) and derived parameters—and we present the distribution of all parameters for the entire FRB data set in Figure 1. We choose 10 observational parameters, as was done by B. H. Chen et al. (2022):

1. Boxcar width $\Delta t_{\rm bc}$ (ms)—the boxcar width of the burst, with the label name "*bc_width*" in the two catalogs.
2. Width of the burst $\Delta t_{\rm fitb}$ (ms)—the width of the burst that is fitted by `fitburst`,[4] with the label name "*width_fitb*" in the two catalogs.
3. Flux S_ν (Jy)—the peak flux of the band average profile (lower limit) with the label name "*flux*" in the two catalogs.
4. Fluence F_ν (Jy · ms)—the flux integrated over the duration of the burst (lower limit) with the label name "*fluence*" in the two catalogs.
5. Scattering time $\Delta t_{\rm sc}$ (ms)—the scattering time at 600 MHz of the burst, with the label name "*scat_time*" in the two catalogs.
6. Spectral index γ—the spectral shape parameter of the burst. The label name in the two catalogs is "*sp_idx*."
7. Spectral running r—this value characterizes the frequency dependence of the spectral shape and is labeled as "*sp_run*" in both catalogs.

[4] https://github.com/CHIMEFRB/fitburst

8. Highest frequency $\nu_{\rm max}$ (MHz)—the highest-frequency band of detection for the burst at full-width tenth-maximum. The label name in the two catalogs is "*high_freq*."
9. Lowest frequency $\nu_{\rm min}$ (MHz)—the lowest-frequency band of detection for the burst at full-width tenth-maximum. The label name in the two catalogs is "*low_freq*."
10. Peak frequency ν_p (MHz)—the peak frequency for the burst that is labeled as "*peak_freq*" in both catalogs.

For $\Delta t_{\rm bc}$, $\Delta t_{\rm fitb}$, S_ν, F_ν, and $\Delta t_{\rm sc}$, we take their logarithmic values throughout this work. Cat1 and Cat2023 only provide upper limits for the width of the burst and scattering time for some FRBs, so we opted to use these upper limits in our analysis.

For the derived parameters, we choose six physical properties of FRBs (for further details, see J.-M. Zhu-Ge et al. 2023):

1. Redshift z—the redshifts of FRBs are numerically derived from their DMs.

   In astronomical observations, distance plays a crucial role in analyzing the origins of FRBs. The DM, indicating the total column density of free electrons along the line of sight, serves as a key distance-related parameter. For most FRBs, DM values far exceed those predicted for the Milky Way, pointing to their extragalactic origins. The DMs of FRBs can be separated into different components (see, e.g., W. Deng & B. Zhang 2014; H. Gao et al. 2014; B. Zhou et al. 2014; Y.-P. Yang & B. Zhang 2016; Y.-P. Yang et al. 2017; Z. Li et al. 2019; J.-J. Wei et al. 2019; D.-C. Qiang et al. 2020, 2022; D.-C. Qiang & H. Wei 2020, 2021):

$$\begin{aligned}{\rm DM_{obs}} &= {\rm DM_{MW}} + {\rm DM_{halo}} + {\rm DM_{IGM}} \\ &\quad + {\rm DM_{host}}/(1+z), \end{aligned} \tag{1}$$

   where $\rm DM_{MW}$, $\rm DM_{halo}$, $\rm DM_{IGM}$, and $\rm DM_{host}$ represent the contributions from the Milky Way, the Milky Way halo, the intergalactic medium (IGM), and the host galaxy (including the interstellar medium of the host galaxy and the plasma around the source) of the FRB. In the literature, we usually use the extragalactic DM for research:

$$\begin{aligned}{\rm DM_E} &= {\rm DM_{obs}} - {\rm DM_{MW}} - {\rm DM_{halo}} \\ &= {\rm DM_{IGM}} + {\rm DM_{host}}/(1+z). \end{aligned} \tag{2}$$

   In this paper, the values of $\rm DM_{obs}$ are provided by both catalogs, with the label name "*bonsai_dm*." We used the values of $\rm DM_{MW}$ as provided in Cat1 and Cat2023, which were estimated using the NE2001 model (J. M. Cordes & T. J. W. Lazio 2002; the corresponding label names in Cat1 and Cat2023 are "*dm_exc_ne2001*" and "*dm_exc_1_ne2001*," respectively). Following the previous studies, we adopt $\rm DM_{halo} = 30\,pc\,cm^{-3}$ and $\rm DM_{host} = 70\,pc\,cm^{-3}$. For the $\rm DM_{IGM}$, it can be written as (see, e.g., W. Deng & B. Zhang 2014; Y.-P. Yang & B. Zhang 2016; Z. Li et al. 2019; J.-J. Wei et al. 2019; D.-C. Qiang et al. 2020, 2022; D.-C. Qiang & H. Wei 2020, 2021)

$${\rm DM_{IGM}}(z) = \frac{3cH_0\Omega_{b,0}}{8\pi G m_p}\int_0^z \frac{f_{\rm IGM}(\tilde{z})f_e(\tilde{z})(1+\tilde{z})d\tilde{z}}{E(\tilde{z})}, \tag{3}$$

   where c is the speed of light, G is the gravitational constant, m_p is the mass of the protons, and $E(z)$ is the dimensionless Hubble parameter. For cosmological parameters, we adopt $H_0 = 67.4\,{\rm km\,s^{-1}\,Mpc^{-1}}$, $\Omega_m = 0.315$, and $\Omega_{b,0}h^2 = 0.0224$, from the latest Planck 18 results for the flat ΛCDM cosmology (Planck Collaboration et al. 2020). $f_e(z)$ is the ionized electron number fraction per baryon, and $f_{\rm IGM}(z)$ is the fraction of the baryon mass in the IGM. In principle, these two parameters are functions of the redshift z. In this work, we follow, e.g., D.-C. Qiang et al. (2020), D.-C. Qiang & H. Wei (2021), H. Gao et al. (2014), and Y.-P. Yang et al. (2017), using the fiducial values $f_e = 0.875$ and $f_{\rm IGM} = 0.83$. According to Equations (2) and (3), we can derive the redshifts of all FRBs. Following J.-M. Zhu-Ge et al. (2023), we also set a minimum redshift of 0.002248, corresponding to a luminosity distance of 10 Mpc, to avoid zero or negative values.

   a. Rest-frame frequency width $\Delta\nu$ (MHz)—the frequency width corrected for the cosmological redshift effect, which can be calculated by

$$\Delta\nu = (\nu_{\rm max} - \nu_{\rm min})(1+z). \tag{4}$$

   b. Rest-frame width $\Delta t_{\rm rw}$ (ms)—the width of the burst $\Delta t_{\rm fitb}$ corrected for the cosmological redshift effect: $\Delta t_{\rm rw} = \Delta t_{\rm fitb}/(1+z)$. We take the logarithmic values.

   c. Burst energy E (erg)—the energy of an FRB can be calculated by

$$E = \frac{4\pi d_L^2}{1+z} F_\nu \nu_p, \tag{5}$$

   where d_L is the luminosity distance. We take their logarithmic values.

   d. Luminosity L ($\rm erg\,s^{-1}$)—the luminosity of FRBs can be derived from

$$L = 4\pi d_L^2 S_\nu \nu_p, \tag{6}$$

   and we take the logarithmic values.

   e. Brightness temperature T_B (K)—the brightness temperature can be derived as (J.-W. Luo et al. 2022)

$$\begin{aligned} T_B &= \frac{S_\nu d_L^2}{2\pi\kappa_B(\nu_p\Delta t_{\rm fitb})^2} = 1.1\times10^{35}\,{\rm K}\left(\frac{S_\nu}{\rm Jy}\right)\left(\frac{d_L}{\rm Gpc}\right)^2 \\ &\quad\times\left(\frac{\nu_p}{\rm GHz}\right)^{-2}\left(\frac{\Delta t_{\rm fitb}}{\rm ms}\right)^{-2}\frac{1}{1+z}, \end{aligned} \tag{7}$$

   where $\kappa_{\rm B}$ is the Boltzmann constant. We take the logarithmic values.

3. Method

Dimensionality reduction and clustering are two types of unsupervised machine learning methods used in this paper. First, we apply the dimensionality reduction algorithm to automatically convert high-dimensional data into low-dimensional

data. Then, we use a clustering algorithm to cluster the reduced-dimensional data based on their similarities.

3.1. Machine Learning Techniques

3.1.1. Dimensionality Reduction

In this study, we use Uniform Manifold Approximation and Projection (UMAP; L. McInnes et al. 2018), implemented via the Python package `umap-learn`,[5] to perform dimensionality reduction. UMAP is a dimensionality reduction technique that can be used for both visualization and general nonlinear dimensionality reduction. This algorithm assumes that the input data are uniformly distributed on a Riemannian manifold with a locally constant (or approximately constant) Riemannian metric and that the manifold is locally connected. Based on these assumptions, the manifold can be modeled using a fuzzy topological structure.

The use of UMAP has been extensively explored in many studies (e.g., J.-M. Zhu-Ge et al. 2022; B. H. Chen et al. 2023; B. J. R. Raquel et al. 2023; X. Yang et al. 2023). For FRB classification, the three parameters `n_components`, `n_neighbors`, and `min_dist` have a more significant impact on the classification results. Meanwhile, we also experimented with modifying other parameters and found that they had a minimal effect on the classification outcomes. Therefore, in this study, we choose to focus on adjusting these three parameters of UMAP. `n_components` allows us to determine the dimensionality of the reduced space where the data will be embedded. In our work, we set `n_components` = 2 for all features, projecting the data onto a 2D plane for visual representation. `n_neighbors` controls how UMAP balances the local and global structures of the data. UMAP achieves this by controlling the size of the local neighborhood it considers when attempting to learn the underlying structure of the data. This means that low values of `n_neighbors` will cause UMAP to focus on very local structures, potentially at the cost of missing the overall global structure. On the other hand, higher values of `n_neighbors` will push UMAP to consider larger neighborhoods around each point, capturing the broader structure of the data but possibly losing finer details. `min_dist` decides how tightly UMAP can pack points together in low-dimensional space. Basically, it sets the minimum distance between points in the low-dimensional space. Lower values of `min_dist` will lead to more tightly packed, "clumpier" embeddings, which can be beneficial for identifying clusters or preserving finer topological details. In contrast, higher values of `min_dist` will prevent the points from being tightly packed, instead focusing on maintaining the broader topological structure. We scan `n_neighbors` from 2 to 50 and `min_dist` from 0.0 to 0.99. In this paper, we take `n_neighbors` = 21 and `min_dist` = 0.03.

3.1.2. Clustering Algorithms

In this work, we used *k*-means (J. MacQueen et al. 1967; S. Lloyd 1982) and Hierarchical Density-Based Spatial Clustering of Applications with Noise (HDBSCAN; R. J. G. B. Campello et al. 2013, 2015; L. McInnes et al. 2017) to group the reduced-dimensional data into different clusters. *K*-means clustering is based on the distance between each data point and its corresponding cluster center. It aims to minimize the distance between the points and their respective centers, effectively grouping similar points into clusters based on proximity in the feature space. Initially, the *k*-means algorithm selects *k* random points as the initial cluster centers, calculates the Euclidean distance of each data point from these centers, and assigns each point to the nearest center. Then, it recalculates the mean of each cluster, updating the cluster centers. This process is repeated iteratively until the cluster centers stabilize, minimizing the overall variance within the cluster (for details, see S. Fotopoulou 2024 and references therein). We use `sklearn.cluster.KMeans`[6] as the *k*-means clustering algorithm. The essential hyperparameter is `n_clusters`, which means how many clusters are present in the model.

HDBSCAN is a clustering algorithm developed by R. J. G. B. Campello et al. (2013, 2015). It extends Density-based Spatial Clustering of Applications with Noise (DBSCAN; M. Ester et al. 1996) by transforming it into a hierarchical clustering method (J. Han et al. 2012). The algorithm then extracts flat clusters from this hierarchy, based on the stability of the clusters, which allows it to better handle varying densities and identify clusters of different shapes and sizes. HDBSCAN uses minimum spanning trees, allowing it to discover clusters with varying densities, unlike DBSCAN, which assumes a constant density across the entire data set. This flexibility enables HDBSCAN to identify clusters of different shapes and sizes, making it more adaptable to complex structures. We use a Python package `hdbscan`[7] as this clustering algorithm. The hyperparameters of HDBSCAN adjusted in this paper are `min_cluster_size` and `min_samples`. `min_cluster_size` controls the minimum number of points required to form a cluster, while `min_samples` determines how conservative the algorithm is in classifying points as noise or part of a cluster. These parameters directly influence the number of clusters and the overall shape of the clustering.

To improve the clustering results, we optimize the hyperparameters of the clustering algorithm by maximizing the mean silhouette coefficient[8](P. J. Rousseeuw 1987) across all samples. The silhouette coefficient measures how well a sample fits within its assigned cluster, with values ranging from −1 to 1. Higher values indicate more tightly grouped, well-defined clusters. We show the mean silhouette coefficients changed with the hyperparameters of the clustering algorithm in Figure 2. In this work, we chose the hyperparameters with max mean silhouette coefficients, which are `n_clusters` = 3 for *k*-means and `min_cluster_size` = 37[9] and `min_samples` = 3 for HDBSCAN. We also include the condensed tree of HDBSCAN in Appendix A, to highlight the persistence and stability of the clustering results.

[5] https://github.com/lmcinnes/umap

[6] https://scikit-learn.org/stable/modules/generated/sklearn.cluster.KMeans.html

[7] https://hdbscan.readthedocs.io/en/latest/index.html

[8] https://scikit-learn.org/stable/modules/generated/sklearn.metrics.silhouette_score.html

[9] In fact, when we fixed `min_samples` at 3, the mean silhouette coefficients remained constant as `min_cluster_size` varied from 37 to 60. However, the number of noise points increased during this range. Therefore, we chose `min_cluster_size` = 37 for this study.

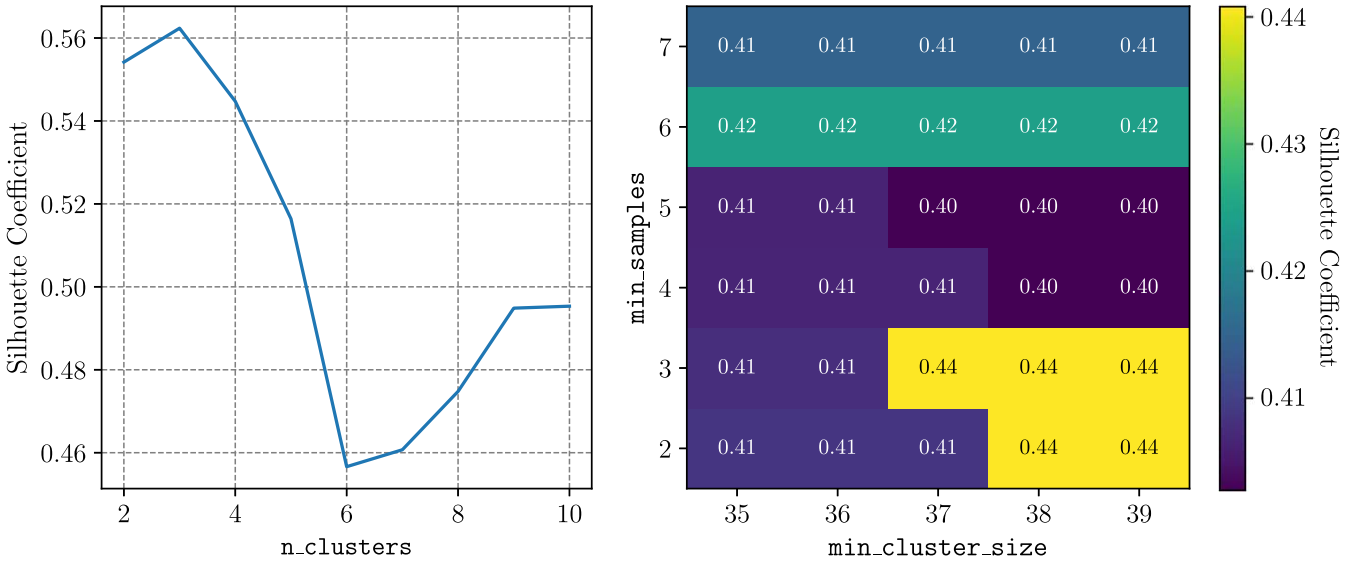

Figure 2. The mean silhouette coefficients of *k*-means (left) and HDBSCAN (right) with respect to different hyperparameters.

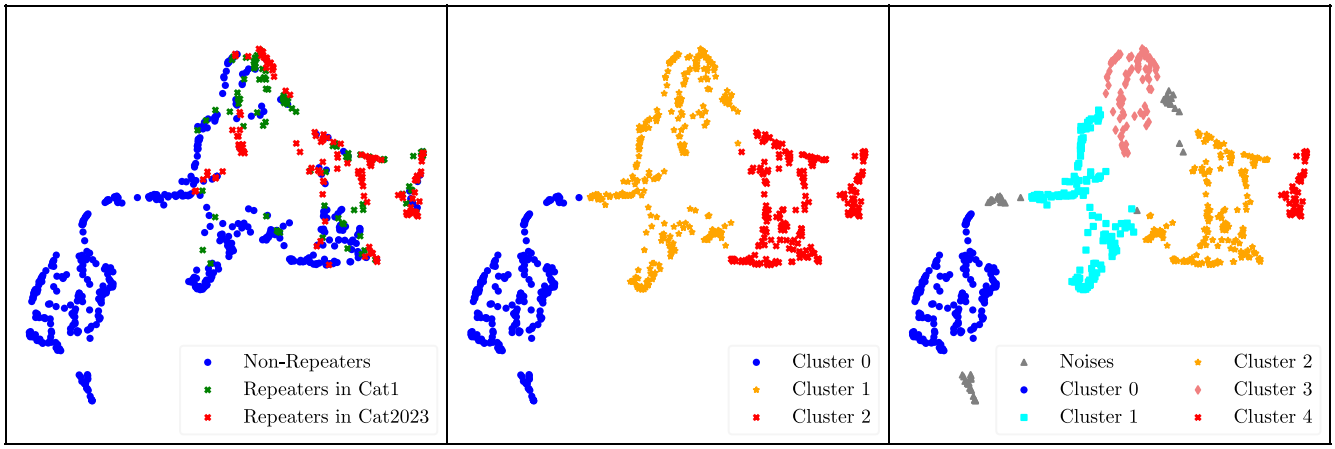

Figure 3. The results of dimensionality reduction and clustering. Left: the distribution of the UMAP embedded data. The blue dots represent nonrepeaters, while the green and red crosses indicate repeaters from Cat1 and Cat2023, respectively. Middle: the clustering result of the UMAP embedded data from *k*-means. Clusters 0, 1, and 2 are represented by the blue dots, orange stars, and red crosses, respectively. Right: the clustering result of the UMAP embedded data from HDBSCAN. The gray triangles, blue dots, cyan squares, orange stars, light coral diamonds, and red crosses represent noise and Clusters 0, 1, 2, 3, and 4, respectively.

3.2. Evaluation Metrics

In this study, we experimented with various machine learning algorithms and hyperparameters, and their classification performance requires evaluation using specific metrics. The outputs of clustering can be written as the following forms:

1. *TP*. The true positives, meaning the number of repeaters correctly classified in the repeater cluster.
2. *TN*. The true negatives, representing the number of nonrepeaters correctly classified in the nonrepeater cluster.
3. *FP*. The false positives, representing the number of nonrepeaters incorrectly classified in the repeater cluster.
4. *FN*. The false negatives, indicating the number of repeaters incorrectly classified in the nonrepeater cluster.

Generally, based on the four outputs mentioned above, various metrics can be calculated to evaluate the model's performance:

1. Recall: $TP/(TP + FN)$.
2. Precision: $TP/(TP + FP)$.
3. Accuracy: $(TP + TN)/(TP + TN + FP + FN)$.

In this study, we use recall to evaluate the model's performance, as observational limitations prevent the accurate determination of nonrepeaters, making it impossible to reliably estimate *TN* and *FP*.

4. Results and Discussion

4.1. Dimensionality Reduction and Clustering

Based on the methods and hyperparameters discussed in Section 3.1.1, we present the UMAP dimensionally reduced features of 745 FRBs in the left panel of Figure 3. The blue dots represent nonrepeaters, while the green and red crosses indicate repeaters from Cat1 and Cat2023, respectively. It is evident that after dimensionality reduction by UMAP, the repeaters are clustered in the upper right corner, while a distinct group of pure nonrepeaters appears in the lower left corner, separated by a noticeable gap from the mixture. This indicates that the 16 parameters of FRBs used in the analysis have the ability to distinguish between nonrepeaters and repeaters.

Table 1
The Clustering Results of the UMAP Embedded Data Using *k*-means and HDBSCAN

Algorithm	Cluster	Nonrepeater Number	Repeater Number	Repeater Candidate Number	Total Number	Repeater Burst Percentage	Recall	Repeater Source Percentage
k-means	Cluster 0	210	0	0	210	0%	100%	61.7%
	Cluster 1	0	98	196	294	33.3%		
	Cluster 2	0	132	103	235	56.2%		
HDBSCAN	Noise	45	14	0	59	23.7%	93.5%	37.0%
	Cluster 0	169	0	0	169	0%		
	Cluster 1	138	15	0	153	9.8%		
	Cluster 2	0	88	118	206	42.7%		
	Cluster 3	0	66	28	94	70.2%		
	Cluster 4	0	47	11	58	81.0%		

Note. For a detailed description, see Section 4.1.

Then we used two types of clustering algorithms—*k*-means and HDBSCAN—to cluster the 2D UMAP embedding. We present the clustering results in the middle and right panels of Figure 3, based on the hyperparameters of *k*-means and HDBSCAN discussed in Section 3.1.2. If the proportion of repeaters in a cluster exceeds 30%, we classify it as a "repeater cluster," with the nonrepeaters within it considered as "repeater candidates." Conversely, if the proportion is below 30%, it is classified as an "nonrepeater cluster."

As shown in the middle panel of Figure 3, the *k*-means algorithm divided the UMAP embedded data into three clusters. Cluster 0 contains 210 FRBs, all of which are nonrepeaters. Cluster 2 consists of 294 FRBs, including 98 repeaters and 196 repeater candidates (the repeater burst percentage is 33.3%). Cluster 3 contains 235 FRBs, with 132 repeaters (the repeater burst percentage is 56.2%) and 103 repeater candidates. All repeaters are classified into repeater clusters, giving a recall of 100%. Out of the 509 nonrepeaters, 299 repeater candidates were identified (from 269 nonrepeater sources). If these repeater candidates are real, the repeater source percentage of FRBs would reach approximately 61.7%, exceeding the predicted rates from studies such as B. H. Chen et al. (2022), J.-M. Zhu-Ge et al. (2022), and X. Yang et al. (2023).

As shown in the right panel of Figure 3, HDBSCAN divided the UMAP embedded data into five clusters and a noise cluster. Cluster 0 contains 169 FRBs, all of which are nonrepeaters. Cluster 1 includes 15 repeaters and 138 nonrepeaters, with repeater bursts making up only 9.8%. Clusters 2, 3, and 4 contain 206, 94, and 58 FRBs, with 88, 66, and 47 repeaters (repeater burst percentages accounting for 42.7%, 70.2%, and 81.0%, respectively) and repeater candidates numbering 118, 28, and 11 (a total of 157 candidates, corresponding to 141 nonrepeater sources). The recall for the 739 samples is 93.1%. The overall repeater source percentage is around 37.9%, slightly lower than the results of S. Yamasaki et al. (2023) and K. McGregor & D. R. Lorimer (2024) but comparable to those of B. H. Chen et al. (2022), J.-M. Zhu-Ge et al. (2022), and X. Yang et al. (2023). Detailed clustering results for both algorithms are also presented in Table 1.

We plot the feature distributions of different clusters generated by *k*-means and HDBSCAN in Figures 4 and 5, respectively. As shown in Figure 4, the rest-frame frequency width differs the most across clusters, indicating that repeater clusters tend to have narrower-frequency bandwidths. Significant differences are also observed in the distributions of the spectral index, highest frequency, redshift, energy, luminosity, and brightness temperature among the clusters. These results are consistent with the feature distribution of repeaters and nonrepeaters shown in Figure 1. In Figure 5, almost all features show notable differences in their distributions among clusters, with the rest-frame frequency width once again being the most distinct, similar to the results in Figure 4.

As mentioned in Section 2, there are six FRB sources that were previously observed as nonrepeaters in Cat1 but were later identified as repeaters in Cat2023. We mark these six FRBs in Figure 6 with green open stars to analyze the reliability of our repeater candidate predictions. The left and right panels of Figure 6 show the repeater candidate predictions from *k*-means and HDBSCAN, respectively. For *k*-means, five out of these six FRB sources are located in the repeater clusters and were successfully identified as repeater candidates, while HDBSCAN predicted four of them successfully. This indicates that our method is effective in identifying potential repeaters. However, one of these six FRBs stands out—FRB 20180910A—which was classified into the nonrepeater cluster by both clustering algorithms. After analyzing its 16 parameters, we found that its boxcar width is only 0.98 ms, and its spectral index (0.05) and spectral running (−0.53) are very similar to those of nonrepeaters. Additionally, its broadband emission characteristics differ significantly from the narrowband emission typically observed in repeaters. Currently, there is no satisfactory theoretical explanation for repeaters that exhibit characteristics so similar to nonrepeaters. We also found that FRB 20180910A has so far produced three detected bursts, with intervals of 1 yr and 9 months. These bursts exhibit noticeable differences in boxcar width, bandwidth, spectral index, and spectral running. It is possible that these bursts are from different nonrepeaters within the same galaxy (or neighboring galaxies in the same direction). Further observations are needed to confirm this.

Regarding FRB 20190226B, which was misidentified only by HDBSCAN, we analyzed its 16 parameters and found no distinct characteristics suggesting it is a nonrepeating burst.

Additionally, some of the nonrepeaters from Cat1 have identified host galaxies (C. J. Law et al. 2020; M. Bhardwaj et al. 2024). In both panels of Figure 6, we highlight two of these FRBs (FRB 20181220A and FRB 20190418A) that were identified as repeater candidates by both clustering algorithms, with black circles. Continued observations of the host galaxies of these two FRBs may reveal further repeating bursts in the future.

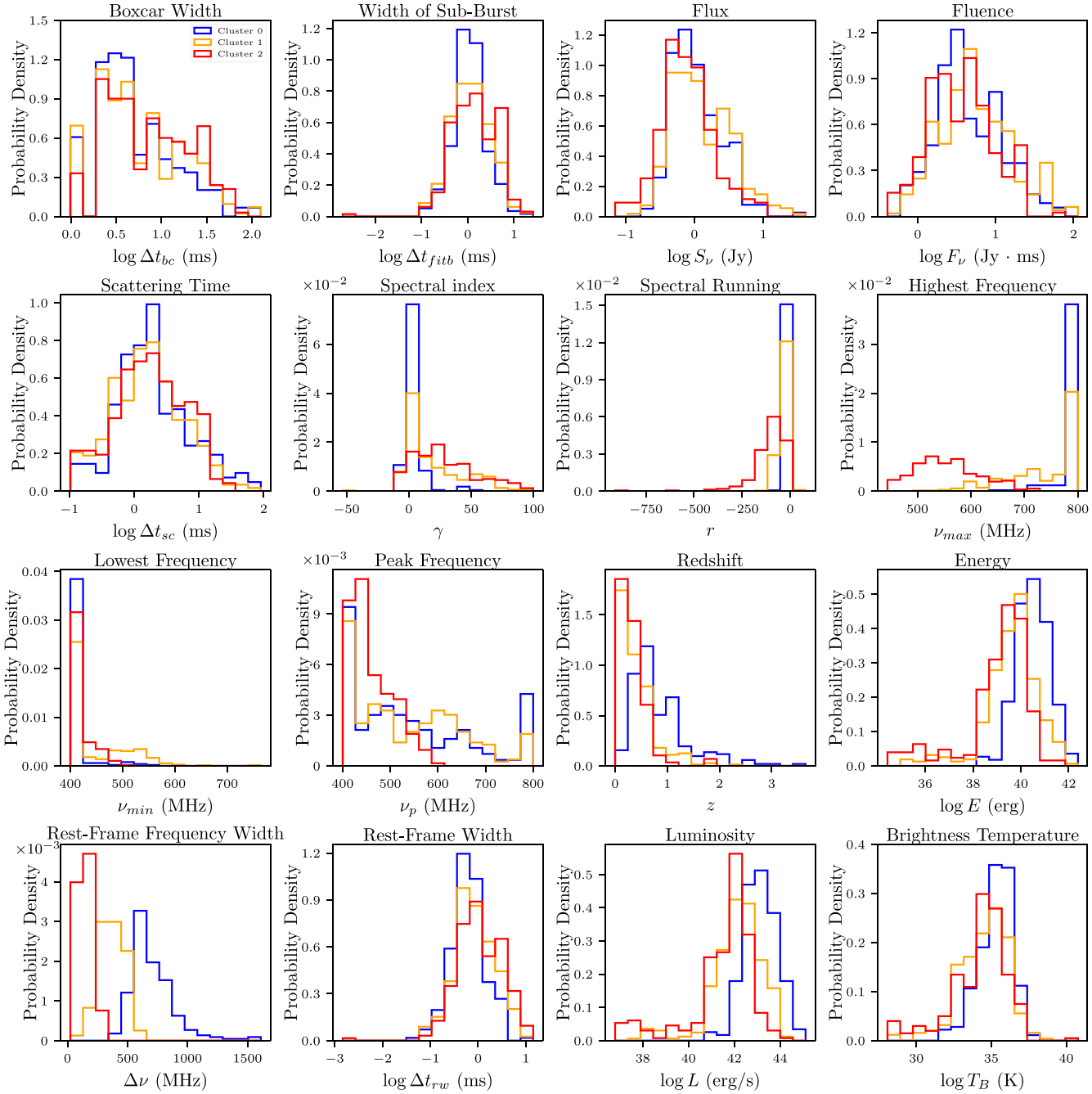

Figure 4. The distributions of 16 parameters across different clusters from *k*-means are illustrated, with the blue, orange, and red histogram step lines representing Cluster 0, Cluster 1, and Cluster 2, respectively.

4.2. Empirical Relationships

In this paper, we further analyze the potential 2D empirical relations within different clusters identified by various clustering algorithms. We pair the 16 parameters of FRBs from different clusters and linearly fit the data points using `scipy.stats.linregress`,[10] which performs linear least-squares regression. The form of the 2D empirical relationship is given as $y = a\,x + b$, and the goodness of fit is evaluated using the score (coefficient of determination), defined as $R^2 = 1 - \sum_i (y_i - \hat{y}_i)^2 / \sum_i (y_i - \bar{y}_i)^2$, where y_i, $\hat{y}_i$, and $\bar{y}_i$ are the observed values, the regressed values, and the mean of the observed values, respectively. The closer R^2 is to 1, the better the model fits the data. To quantify the statistical differences in the slopes and intercepts of the empirical relationships across different clusters, we implemented the Chow test for evaluation (G. C. Chow 1960). The null hypothesis of the Chow test is that the two samples come from the same regression model. If the p-value is less than 0.05, the null hypothesis is rejected, indicating that the two samples come from different regression models.

We set a high-score threshold of $R^2 > 0.5$ to filter out well-fitted empirical relations and excluded parameter combinations that inherently have a linear relationship (e.g., luminosity and flux). For the clusters from *k*-means, the selected empirical

[10] https://docs.scipy.org/doc/scipy/reference/generated/scipy.stats.linregress.html

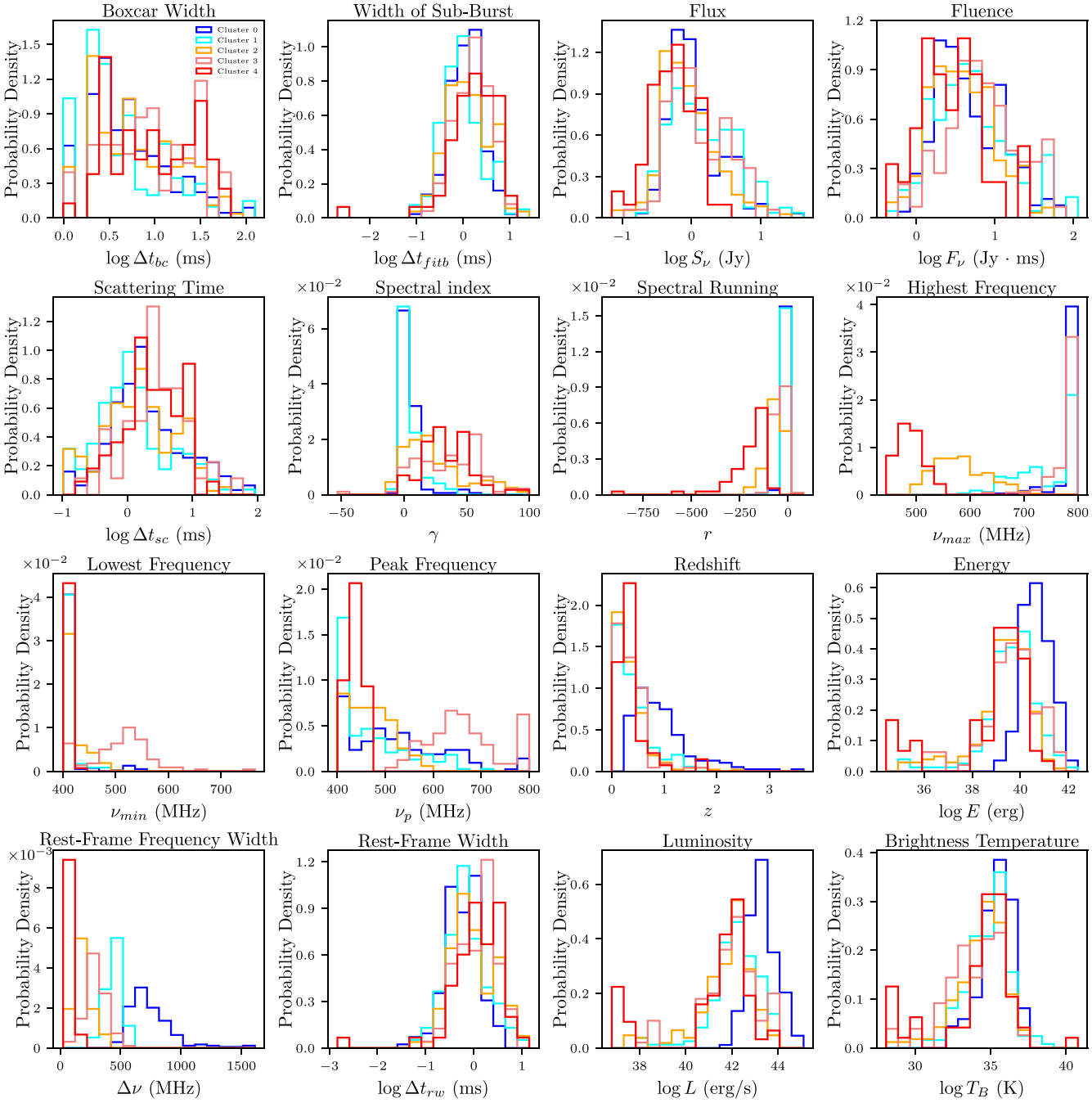

Figure 5. The same as Figure 4 but displaying the results from HDBSCAN. The blue, cyan, orange, light coral, and red histogram step lines represent Clusters 0, 1, 2, 3, and 4, respectively.

relations are shown in Figure 7. The slope, intercept, and score of the empirical relations are listed in Table 2. The p-values of the Chow test between different clusters are listed in Table 3. The left panel of Figure 7 shows the empirical relation between two independent parameters: scattering time ($\log \Delta t_{\rm sc}$) and rest-frame width ($\log \Delta t_{\rm rw}$). We observe that $R^2 > 0.5$ only in Cluster 2, corresponding to a repeater cluster, whereas the $\log \Delta t_{\rm sc} - \log \Delta t_{\rm rw}$ relation appears less significant in the other two clusters. However, the slope and intercept of the relation $\log \Delta t_{sc} - \log \Delta t_{rw}$ are similar in Clusters 1 and 2. Similarly, the p-value of the Chow test between Clusters 1 and 2 is greater than 0.05, indicating that they likely come from the same regression model. This may be because both clusters are repeater clusters. The right panel of Figure 7 displays the empirical relation between two other independent parameters: spectral acceleration (r) and spectral index (γ). In contrast to the $\log \Delta t_{rw} - \log \Delta t_{sc}$ relation, the r–γ relation is less evident in Cluster 2 but is very pronounced in Clusters 0 and 1 ($R^2 > 0.8$), with similar slopes and intercepts. Moreover, the p-value of the Chow test between these two clusters even reaches around 0.5, indicating that some repeaters may share spectral properties with nonrepeaters. Combining the two repeater clusters, Cluster 1 and Cluster 2, the relation $\log \Delta t_{sc} - \log \Delta t_{rw}$ yields an R^2 value of 0.4608. Although this is less than 0.5, it still exhibits a distinct empirical correlation compared to nonrepeating bursts. The r–γ relation

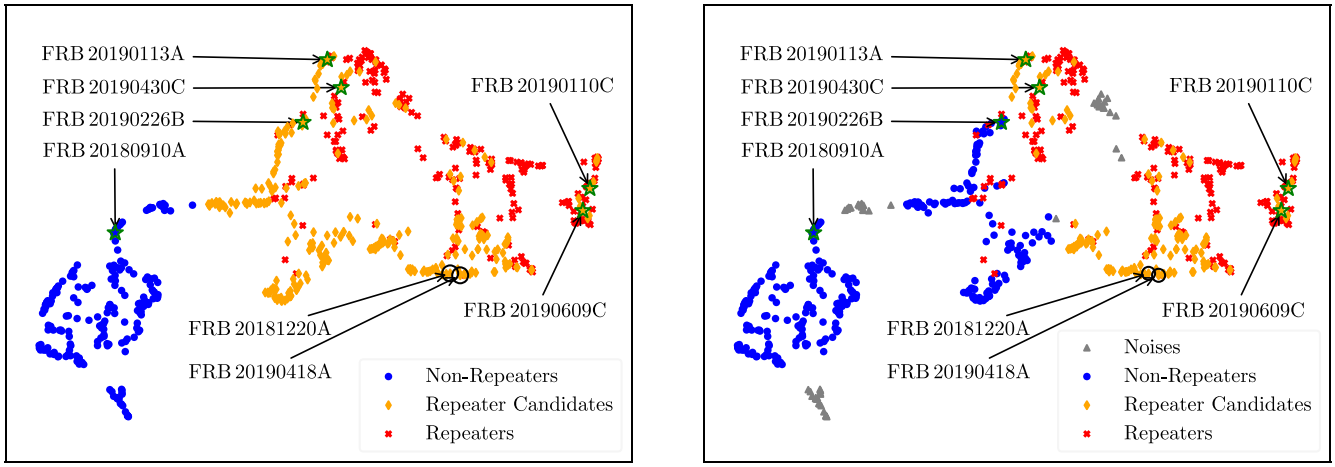

Figure 6. The distribution of nonrepeaters (blue dots), repeater candidates (orange diamonds), and repeaters (red crosses) is presented in the clustered UMAP embedded data from both *k*-means (left) and HDBSCAN (right). The gray triangles represent noises. The green stars mark the first bursts of six repeaters that were misidentified as nonrepeaters in Cat1 but are later identified as repeaters in Cat2023. The black circles indicate the localized nonrepeaters.

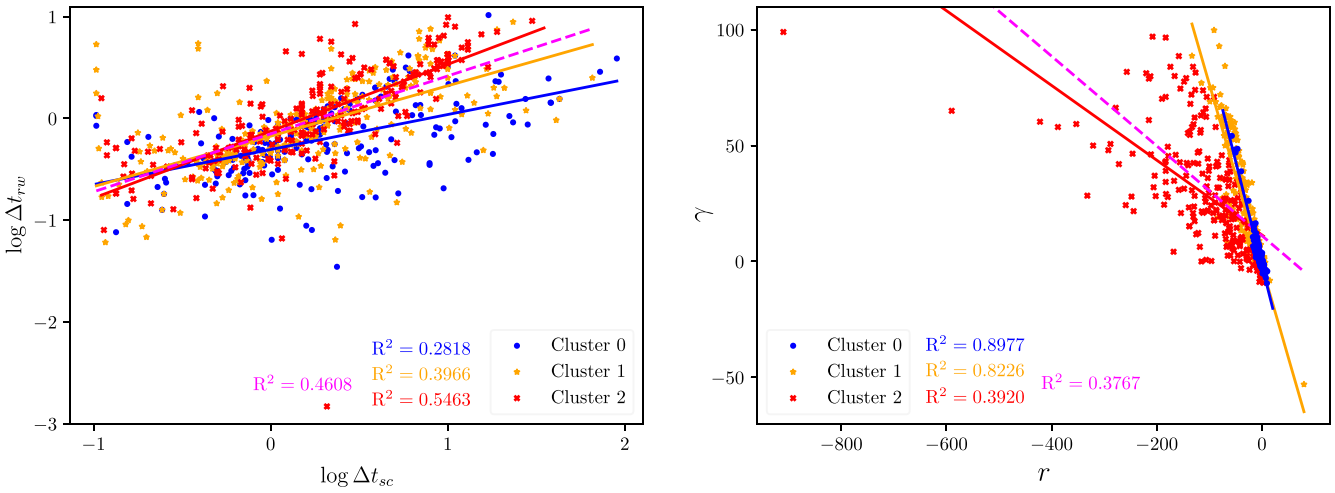

Figure 7. The empirical relationships between scattering time (log Δt_{sc}) and rest-frame width (log Δt_{rw}; left) and between spectral acceleration (r) and spectral index (γ; right) are shown for FRBs in different clusters from *k*-means. These relationships are represented by blue, orange, and red lines, corresponding to Clusters 0, 1, and 2, respectively. The associated R^2 values are shown in the same colors. Additionally, the dashed magenta line and its corresponding R^2 represent the combined data from Clusters 1 and 2. See Section 4.2 for details.

Table 2
The Slope (a), Intercept (b), and R^2 Values of the Empirical Relations for Different Clusters from *k*-means

x	y	Cluster	a	b	R^2
log Δt_{sc}	log Δt_{rw}	0	0.3440	−0.3055	0.2818
		1	0.4954	−0.1744	0.3966
		2	0.6572	−0.1256	0.5463
		[1, 2]	0.5691	−0.1519	0.4608
r	γ	0	−0.9000	−1.6846	0.8977
		1	−0.7853	−1.9914	0.8226
		2	−0.1613	11.4422	0.3920
		[1, 2]	−0.1936	11.1439	0.3767

Table 3
The p-values of Chow Tests for *k*-means Clusters

	p-value	
	Relation	
Clusters	log Δt_{sc} − log Δt_{rw}	r–γ
0 and 1	0.0016	0.5177
0 and 2	1.75e–06	6.28e–05
1 and 2	0.1975	1.11e–16
0 and [1, 2]	2.49e–06	0.0190

for the combined clusters has an R^2 value of 0.3767, which is even lower than that of Cluster 2. This may result from the substantial disparity between the r–γ relations of Cluster 1 and Cluster 2, as well as the relatively weak correlation observed in Cluster 2. The p-values of the Chow test between the nonrepeater cluster (Cluster 0) and the repeater clusters (Clusters 1 and 2) are all below 0.05 for both empirical relations. This result strengthens the idea that FRBs can be classified into repeaters and nonrepeaters.

Figure 8 shows the empirical relations for different clusters from HDBSCAN, and Table 4 lists the slope, intercept, and score of these empirical relations. The p-values of the Chow test between different clusters are listed in Table 5. The left

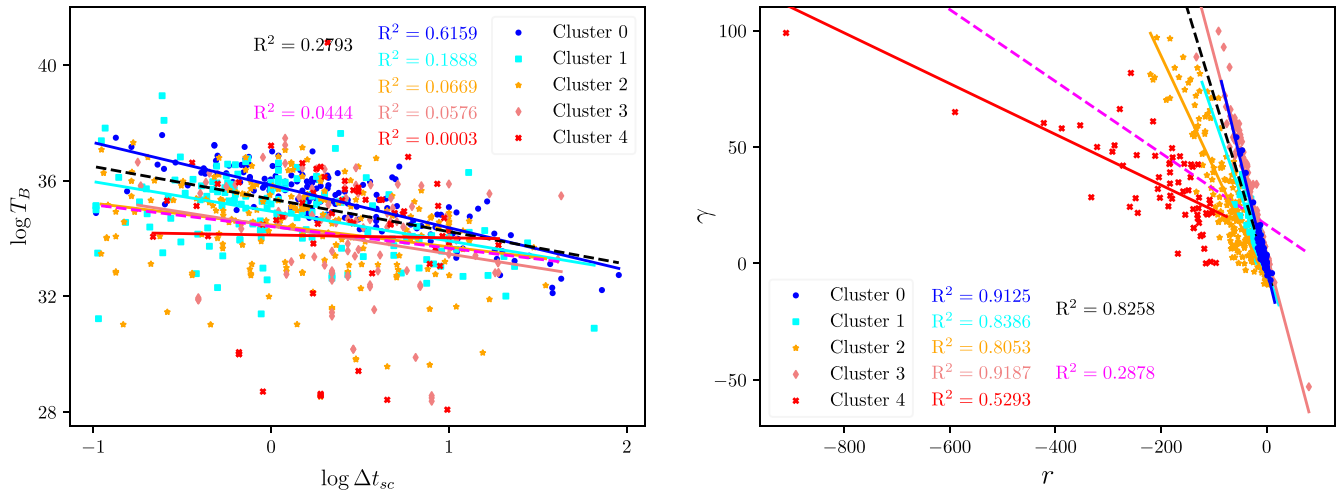

Figure 8. The empirical relationships between scattering time (log Δt_{sc}) and brightness temperature (log T_B; left) and between spectral acceleration (r) and spectral index (γ; right) are shown for FRBs in different clusters from HDBSCAN. These relationships are represented by the blue, cyan, orange, light coral, and red lines, corresponding to Clusters 0, 1, 2, 3, and 4, respectively. The associated R^2 values are shown in the same colors. Additionally, the dashed black (magenta) line and its corresponding R^2 represent the combined data from Clusters 0 and 1 (2, 3, and 4). See Section 4.2 for details.

Table 4
The Slope (a), Intercept (b), and R^2 Values of the Empirical Relations for Different Clusters from HDBSCAN

x	y	Cluster	a	b	R^2
log Δt_{sc}	log T_B	0	−1.4741	35.8475	0.6159
		1	−1.0264	34.9418	0.1888
		2	−0.7559	34.4684	0.0669
		3	−0.9667	34.4318	0.0576
		4	−0.098	34.1223	0.0003
		[0, 1]	−1.1274	35.3659	0.2793
		[2, 3, 4]	−0.7510	34.4152	0.0444
r	γ	0	−0.9394	−2.2495	0.9125
		1	−0.6574	−2.6236	0.8386
		2	−0.4835	−7.4780	0.8053
		3	−0.8527	4.4482	0.9187
		4	−0.1090	11.8615	0.5293
		[0, 1]	−0.7424	−2.1286	0.8258
		[2, 3, 4]	−0.1542	16.5526	0.2878

Table 5
The p-values of Chow Tests for HDBSCAN Clusters

	p-value	
	Relation	
Cluster	log Δt_{sc} − log T_B	r–γ
0 and 1	0.0041	1.13e–10
0 and 2	0.1701	1.75e–09
0 and 3	0.0483	0.4561
0 and 4	0.5232	1.11e–16
1 and 2	0.2403	0.0019
1 and 3	8.12e–07	6.34e–12
1 and 4	0.0014	1.11e–16
2 and 3	0.0002	1.11e–16
2 and 4	0.0379	1.11e–16
3 and 4	0.6024	1.11e–16
[0, 1] and [2, 3, 4]	2.43e–11	1.97e–08

panel displays the relation between the rest-frame width (log Δt_{sc}) and the brightness temperature (log T_B), which are also two independent parameters. We can see that only Cluster 0 (a nonrepeater cluster) has a significant log Δt_{sc} − log T_B relation with $R^2 > 0.6$, while the other clusters show no strong log Δt_{sc} − log T_B relation. Even if the p-values of the Chow test between some clusters are greater than 0.05, this does not necessarily indicate that they originate from the same regression model. The right panel shows the empirical relation between spectral acceleration (r) and spectral index (γ). All clusters exhibit a significant r–γ relation, especially Clusters 0–3, where $R^2 > 0.8$. Notably, Clusters 0 and 3 (a repeater cluster) have very similar slopes and intercepts for the r–γ relation (the p-value of the Chow test is 0.45), suggesting that certain repeaters might have spectral properties similar to those of nonrepeaters, a trend also observed in the k-means results. We also analyzed the relations using the combined data from Clusters 0 and 1 (nonrepeater clusters) as well as from Clusters 2, 3, and 4 (repeater clusters). For the log Δt_{sc} − log T_B relation, the R^2 value for the nonrepeater clusters is less than 0.5, likely due to the scattered data in Cluster 1. However, it still performs better than the repeater cluster, which has an R^2 value of 0.0444, indicating that the log Δt_{sc} − log T_B relation is virtually nonexistent for the repeater cluster. The r–γ relation is still apparent in the nonrepeater clusters, but the R^2 value is less than 0.5 in the repeater clusters. This may be due to the significant differences in slope and intercept of the r–γ relation across Clusters 2, 3, and 4. The p-values of the Chow test between nonrepeater clusters and repeater clusters are all significantly below 0.05 for both empirical relations, aligning with the results from k-means clustering.

5. Conclusion and Future Prospects

Machine learning is a powerful tool for classifying FRBs. In this paper, we applied unsupervised learning methods, including dimensionality reduction and clustering algorithms, to

differentiate between repeaters and nonrepeaters in the first CHIME/FRB catalog (CHIME/FRB Collaboration et al. 2021) and the CHIME/FRB Collaboration 2023 catalog (CHIME/FRB Collaboration et al. 2023). We extracted 16 parameters from the FRBs to serve as input features for unsupervised learning, ensuring that the information from the FRBs was sufficiently comprehensive. Ultimately, we successfully identified several candidate repeaters among the nonrepeaters. Using the UMAP + k-means method, we identified 269 nonrepeaters as repeater candidates, with an estimated repeater source percentage of 61.7%. With the UMAP + HDBSCAN method, 141 nonrepeaters were identified as repeater candidates, yielding a repeater source percentage of 37.9%. All repeater candidates are summarized in Appendix B. Additionally, we found that FRBs in repeater clusters and nonrepeater clusters exhibit different distributions across several features, suggesting that repeaters and nonrepeaters may belong to distinct categories.

We used six FRB sources previously classified as nonrepeaters but actually confirmed as repeaters to evaluate the predictive capability of our model. The UMAP + k-means method successfully predicted five of these sources, while the UMAP + HDBSCAN method successfully predicted four. The only exception was FRB 20180910A, which could not be predicted. The reason for this is that many of its characteristics —such as frequency bandwidth, spectral index, and spectral running—closely resemble those of nonrepeaters, making it distinctly different from typical repeaters. Additionally, the intervals between the three outbursts of this repeater are quite long, and the features of each burst show significant variation. This may indicate that the FRB sources are unrelated and originate from different galaxies within the same direction or from different sources in the same galaxy. Furthermore, within Cat1, there are some localized nonrepeaters, and we identified two of them as repeater candidates using both clustering algorithms. Continued observations of the host galaxies of these two FRBs may reveal additional repeating bursts in the future.

We further analyzed the empirical relations that may exist within different clusters. For the clusters derived from k-means, we identified a significant (with $R^2 > 0.5$) $\log \Delta t_{\rm sc} - \log \Delta t_{\rm rw}$ relation exclusive to Cluster 2, as well as an r–γ relation present only in Clusters 0 and 1. For the clusters obtained through HDBSCAN, we found a notable $\log \Delta t_{\rm sc} - \log T_B$ relation that exists solely in Cluster 0, along with the r–γ relation observed across all clusters. The spectral index γ and the spectral running r are the shape parameters of the FRB spectrum, described by a continuous power-law function (Z. Pleunis et al. 2021; Planck Collaboration et al. 2020):

$$I(\nu) = A(\nu/\nu_0)^{\gamma + r\ln(\nu/\nu_0)}, \tag{8}$$

where $I(\nu)$ is the intensity at spectral frequency ν, A is the amplitude, and ν_0 is the pivotal frequency, set at 400.1953125 MHz, the lower limit of the CHIME band. The strict r–γ relation means that only one parameter can determine the morphology of an FRB. Some clusters from k-means exhibit relatively weak but still noteworthy empirical relations, such as the $\log \Delta t_{\rm sc} - \log \Delta t_{\rm rw}$ relation in Clusters 0 and 1 and the r–γ relation in Cluster 2. Similarly, for HDBSCAN, the $\log \Delta t_{sc} - \log T_B$ relation is present but weak in Cluster 1, while it is extremely weak in Clusters 2, 3, and 4, suggesting that it is effectively nonexistent in the latter. These results suggest that the $\log \Delta t_{sc} - \log \Delta t_{rw}$ relation is more pronounced in repeater clusters, whereas the $\log \Delta t_{sc} - \log T_B$ relation is more evident in nonrepeater clusters. While the r–γ relation is significant in both repeaters and nonrepeaters, the noticeable differences in slopes and intercepts across different repeater clusters indicate that repeaters do not form a homogeneous group, and their properties may vary significantly.

We also applied the Chow test to assess statistical differences in the slopes and intercepts of empirical relationships across different clusters. For certain prominent empirical relationships, the Chow test p-values indicate that some repeater and nonrepeater clusters share a common regression model, such as the r–γ relation in Clusters 0 and 1 from k-means and Clusters 0 and 3 from HDBSCAN. This suggests that some repeaters and nonrepeaters exhibit comparable spectral characteristics, a finding consistent with observational evidence—particularly in the case of FRB 20180910A, if it is indeed a genuine repeater. However, this also implies that if some repeaters behave similarly to nonrepeaters in key spectral relationships, some FRBs currently classified as nonrepeaters might actually be repeaters with undetected bursts, due to observational limitations. Subsequently, when all repeater and nonrepeater clusters are merged separately, the Chow test p-values reveal significantly distinct empirical relationships between the two groups, reinforcing the notion that FRBs can indeed be categorized into repeaters and nonrepeaters.

In the future, improvements in observational data and machine learning techniques will refine FRB classification, reduce misclassifications, and uncover more repeaters. The use of advanced clustering algorithms and multiwavelength observations will enhance the accuracy of models, while deep learning approaches may reveal new patterns. These advancements will contribute to a better understanding of the origins and physical mechanisms of FRBs, with potential implications for cosmology.

Acknowledgments

We are grateful to Hao Wei, Jing-Yi Jia, Lin-Y. Li, Jia-Lei Niu, and Yu-Xuan Li for their kind assistance and valuable discussions. D.-C.Q. is supported by the Startup Research Fund of Henan Academy of Sciences No. 241841222. S.Y. acknowledges the funding from the National Natural Science Foundation of China under grant No.12303046 and from the Startup Research Fund of Henan Academy of Sciences No.241841217. J.Z. is supported by funding from the National Natural Science Foundation of China under grant No.12403002 and from the Startup Research Fund of Henan Academy of Sciences No.241841221. Z.-Q.Y. is supported by the National Natural Science Foundation of China under grant No. 12305059, the Joint Fund of Henan Province Science and Technology R&D Program No. 235200810111, and the Startup Research Fund of Henan Academy of Sciences No. 241841224.

Appendix A
Condensed Tree of HDBSCAN

We show the condensed tree of HDBSCAN in Figure 9 to highlight the persistence and stability of the clustering results. λ is used to consider the persistence of clusters, which can be calculated by $\lambda = 1/d$, where d is the distance between a point and cluster core. For a given cluster, $\lambda_{\rm birth}$ marks when the

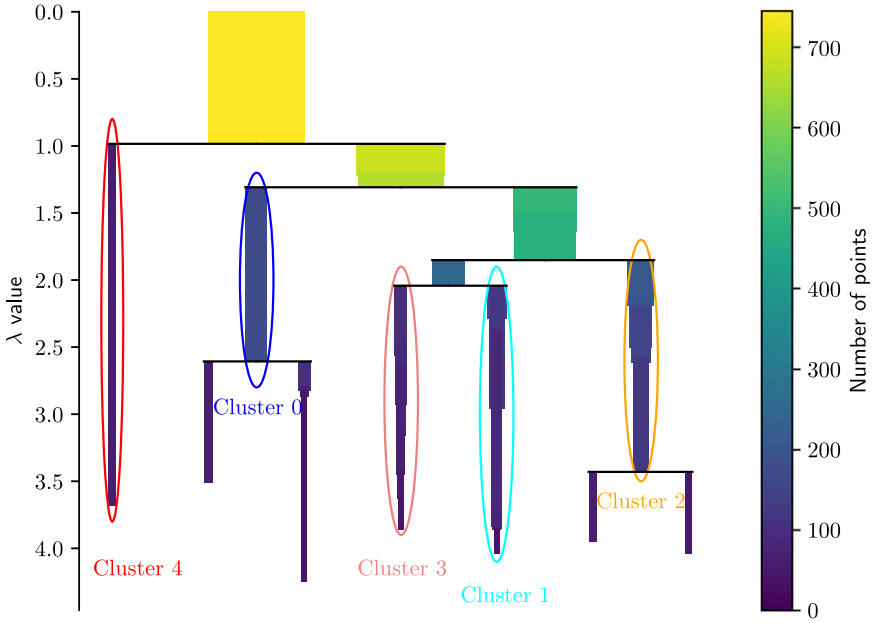

Figure 9. The condensed tree of HDBSCAN. The leaf nodes within the ellipses of different colors represent the final clusters obtained by HDBSCAN, while the other leaf nodes are noise.

cluster first formed, and λ_{death} (if applicable) marks when it split into smaller clusters. For each point p in the cluster, λ_p represents the value at which the point left the cluster, occurring between λ_{birth} and λ_{death}, either during the cluster's lifetime or at the split. Then we can compute the stability for each cluster as $S = \sum_{p \in \text{cluster}}(\lambda_p - \lambda_{\text{birth}})$. Start by declaring all leaf nodes as selected clusters. Move up the tree: if the sum of the child cluster stabilities exceeds the parent cluster's stability, update the parent's stability to this sum. Otherwise, select the parent cluster and deselect its descendants. At the root node, the selected clusters form the flat clustering, which is then returned. Ultimately, we selected the five clusters enclosed within the ellipses in Figure 9. See https://hdbscan.readthedocs.io/en/latest/how_hdbscan_works.html for more details.

Appendix B
Repeater Candidates

Here, we present the repeater candidates identified using unsupervised machine learning methods, listed in Table 6. The "Sub Num" column lists the sub-burst numbers of FRBs from Cat1 and Cat2023. The "Note" column specifies whether each candidate was identified exclusively by k-means ("k") or by both k-means and HDBSCAN ("both").

Table 6
The List of Repeater Candidates

FRB Name	Sub Num	R.A.(J2000) (deg)	Decl. (J2000) (deg)	Δt_{bc} (ms)	Δt_{fitb} (ms)	S_ν (Jy)	F_ν (Jy · ms)	Δt_{sc} (ms)	γ	r	ν_{max} (MHz)	ν_{min} (MHz)	ν_{peak} (MHz)	z	log E (erg)	$\Delta\nu$ (MHz)	Δt_{rw} (ms)	log L (erg s^{-1})	log T_B (K)	Note
FRB 20180725A	0	93.4	67.1	2.95	0.30	1.70	4.10	1.10	38.20	−45.80	760.1	485.3	607.4	0.641	40.45	450.9	0.18	43.28	35.74	*k*
FRB 20180729A	0	199.4	55.6	0.98	0.10	11.70	17.00	0.16	16.46	−30.21	692.7	400.2	525.6	0.002	36.03	293.2	0.10	38.87	32.69	*k*
FRB 20180729B	0	89.9	56.5	1.97	0.31	0.92	1.20	0.66	14.50	−14.60	800.2	441.8	657.5	0.158	38.70	414.9	0.27	41.64	34.50	*k*
FRB 20180801A	0	322.5	72.7	9.83	0.58	1.11	7.90	5.54	60.00	−75.50	709.3	500.2	595.6	0.553	40.60	324.8	0.37	42.94	34.40	both
FRB 20180810B	0	180.4	83.1	0.98	0.31	5.20	7.90	0.20	−0.76	−4.06	778.6	400.2	400.2	0.031	37.86	390.1	0.30	40.70	34.86	*k*
FRB 20180812A	0	19.3	80.8	7.86	1.30	0.93	5.40	2.81	−2.90	−8.30	586.4	400.2	400.2	0.727	40.50	321.6	0.75	42.97	35.10	both
FRB 20180904A	0	286.6	81.2	1.97	0.53	3.80	6.00	0.55	12.12	−23.18	712.3	400.2	519.7	0.257	39.73	392.2	0.42	42.63	35.76	*k*
FRB 20180907A	0	320.9	29.5	5.90	0.87	0.87	2.80	0.26	−2.30	−5.10	648.6	400.2	400.2	0.797	40.30	446.5	0.48	43.04	35.40	*k*
FRB 20180907E	0	167.9	47.1	11.80	4.15	0.73	6.90	3.38	−7.10	−2.70	536.3	400.2	400.2	0.312	39.85	178.5	3.16	41.99	33.89	both
FRB 20180909A	0	123.6	56.8	19.66	6.31	0.33	1.02	8.20	−0.30	−1.30	800.2	400.2	400.2	0.319	39.04	527.5	4.79	41.67	33.12	*k*
FRB 20180911A	0	99.5	84.6	1.97	0.83	1.60	2.60	0.94	−5.78	0.20	599.9	400.2	400.2	0.085	38.26	216.6	0.77	41.09	34.62	both
FRB 20180915A	0	280.6	17.9	4.92	0.80	2.30	6.20	0.88	6.50	−9.10	800.2	400.2	571.9	0.128	39.16	451.1	0.71	41.78	34.04	*k*
FRB 20180915B	0	225.2	25.0	4.92	1.69	0.99	3.80	0.11	−9.20	3.00	527.4	400.2	400.2	0.072	38.28	136.3	1.58	40.73	33.47	both
FRB 20180916A	0	349.0	80.3	0.98	0.10	2.40	4.50	0.19	2.41	−8.10	793.2	400.2	464.7	0.151	39.08	452.2	0.09	41.87	35.79	*k*
FRB 20180920A	0	78.9	28.3	14.75	2.22	0.86	8.50	9.10	20.10	−26.30	787.4	435.9	585.9	0.360	40.24	478.2	1.63	42.38	33.57	*k*
FRB 20180920B	0	191.1	63.5	10.81	2.33	0.35	1.70	1.73	12.30	−121.00	483.4	400.2	421.1	0.401	39.49	116.5	1.66	41.95	33.83	both
FRB 20180921A	0	28.9	5.0	3.93	1.14	0.92	2.30	1.50	1.00	−10.40	672.2	400.2	419.9	0.319	39.42	358.8	0.86	42.14	34.92	*k*
FRB 20180922A	0	342.3	69.7	2.95	0.81	2.60	7.70	0.31	−4.00	−9.20	555.9	400.2	400.2	0.383	40.08	215.3	0.58	42.75	35.83	both
FRB 20180923A	0	327.6	71.9	1.97	0.15	0.76	1.20	0.21	18.20	−57.40	572.9	400.2	468.9	0.026	36.96	177.2	0.15	39.77	33.12	both
FRB 20180923D	0	169.1	48.8	0.98	0.10	2.40	2.20	0.11	20.90	−92.70	524.4	400.2	448.0	0.248	39.20	155.0	0.08	42.33	36.27	both
FRB 20180923C	0	239.1	22.9	1.97	0.32	0.89	1.37	0.50	1.00	−10.20	675.6	400.2	420.5	0.059	37.69	291.7	0.30	40.53	34.01	both
FRB 20180925B	0	145.4	21.0	5.90	1.15	0.76	2.70	1.40	15.00	−41.50	606.9	400.2	479.6	0.623	40.14	335.5	0.71	42.80	34.97	both
FRB 20180928A	0	312.9	30.9	2.95	0.27	1.34	2.50	0.15	−2.93	−39.70	492.1	400.2	400.2	0.002	35.08	92.1	0.27	37.81	31.02	both
FRB 20181012B	0	206.3	64.2	3.93	0.56	0.49	1.44	0.26	20.90	−154.00	483.9	400.2	428.3	0.682	39.90	140.8	0.33	42.66	35.31	both
FRB 20181013A	0	262.8	38.4	0.98	0.51	2.81	3.50	0.56	1.08	−5.20	800.2	400.2	443.7	0.204	39.22	481.5	0.43	42.20	36.16	*k*
FRB 20181013E	0	307.3	69.0	2.95	0.86	0.62	2.03	1.10	−5.60	0.90	623.0	400.2	400.2	0.208	38.96	269.1	0.71	41.52	34.66	both
FRB 20181013B	0	97.2	52.0	119.93	2.80	0.56	21.00	65.60	−0.50	−4.20	790.4	400.2	400.2	0.119	39.47	436.5	2.50	40.95	30.90	*k*
FRB 20181013C	0	146.1	34.1	4.92	0.76	0.44	1.64	0.43	−3.70	−0.80	698.0	400.2	400.2	1.001	40.26	595.8	0.38	42.99	35.46	*k*
FRB 20181014C	0	117.9	41.6	3.93	0.79	0.57	1.48	1.00	18.00	−30.50	707.7	408.6	537.7	0.694	40.03	506.7	0.47	42.84	35.20	*k*
FRB 20181017B	0	237.8	78.5	12.78	2.31	1.06	6.50	4.30	61.00	−77.00	704.8	499.3	593.2	0.207	39.63	248.0	1.91	41.92	33.27	*k*
FRB 20181018B	0	336.8	71.9	0.98	0.48	5.10	7.90	0.50	7.30	−10.45	800.2	400.2	567.4	0.105	39.09	441.9	0.43	41.94	35.62	*k*
FRB 20181018C	0	67.2	37.6	0.98	0.48	2.40	3.30	0.51	−0.61	−7.60	668.2	400.2	400.2	0.208	39.17	323.8	0.39	42.11	36.21	both
FRB 20181022C	0	141.6	83.8	3.93	0.80	0.91	3.20	0.68	2.90	−14.20	664.2	400.2	443.9	0.456	39.90	384.3	0.55	42.52	35.19	*k*
FRB 20181022D	0	179.2	36.5	1.97	0.59	2.90	6.20	0.63	18.20	−14.40	800.2	505.7	754.7	0.473	40.46	433.8	0.40	43.29	35.87	both
FRB 20181022E	0	221.2	27.1	2.95	0.40	0.69	2.08	0.63	8.70	−42.30	560.3	400.2	443.7	0.207	39.01	193.3	0.33	41.61	34.61	both
FRB 20181027A	0	131.9	−4.2	5.90	0.72	4.90	22.00	4.72	−0.40	6.10	800.2	530.0	800.2	0.662	41.33	449.2	0.43	43.90	35.39	both
FRB 20181030C	0	309.8	4.0	0.98	0.61	1.60	5.50	0.74	10.00	−22.20	691.2	400.2	500.9	0.587	40.42	461.7	0.38	43.08	36.76	*k*
FRB 20181030D	0	81.8	16.1	2.95	0.36	2.74	5.90	0.87	1.51	−3.00	800.2	400.2	514.8	0.086	38.74	434.4	0.33	41.45	34.30	*k*
FRB 20181030E	0	135.7	8.9	5.90	0.40	2.00	6.30	0.97	22.30	−69.00	564.8	400.2	470.5	0.013	37.09	166.8	0.39	39.59	31.99	both
FRB 20181101A	0	21.3	53.9	30.47	6.03	0.50	10.70	10.00	16.40	−37.70	636.8	400.2	497.4	1.413	41.46	571.0	2.50	43.51	34.03	*k*
FRB 20181115A	0	143.0	56.4	4.92	1.83	0.44	1.92	2.10	19.60	−62.00	568.4	400.2	468.8	0.972	40.37	331.7	0.93	43.03	35.30	both
FRB 20181116A	0	36.0	4.5	1.97	0.44	4.00	5.23	0.47	2.37	−11.00	704.7	400.2	445.8	0.271	39.65	387.2	0.35	42.64	35.96	*k*
FRB 20181116B	0	232.7	64.9	3.93	0.64	0.74	1.92	0.17	−8.80	−4.70	505.5	400.2	400.2	0.336	39.36	140.6	0.48	42.07	34.92	both
FRB 20181117B	1	81.1	80.0	7.86	1.28	3.60	11.00	1.30	11.40	−31.20	630.4	400.2	480.4	0.449	40.46	333.7	0.88	43.14	35.10	both
FRB 20181119B	0	299.4	31.1	22.61	3.33	4.50	94.00	16.59	2.72	−4.65	800.2	400.2	536.4	0.087	39.98	434.9	3.06	41.69	32.72	*k*

Table 6
(Continued)

FRB Name	Sub Num	R.A.(J2000) (deg)	Decl. (J2000) (deg)	Δt_{bc} (ms)	Δt_{fitb} (ms)	S_ν (Jy)	F_ν (Jy · ms)	Δt_{sc} (ms)	γ	r	ν_{max} (MHz)	ν_{min} (MHz)	ν_{peak} (MHz)	z	log E (erg)	$\Delta\nu$ (MHz)	Δt_{rw} (ms)	log L (erg s^{-1})	log T_B (K)	Note
FRB 20181119C	0	190.1	82.2	0.98	0.45	2.80	3.50	0.48	−1.81	−5.70	657.7	400.2	400.2	0.178	39.06	303.4	0.38	42.03	36.13	both
FRB 20181122A	0	60.0	55.5	2.95	0.68	0.53	1.42	0.18	−4.90	0.60	661.4	400.2	400.2	0.442	39.48	376.7	0.47	42.21	35.27	*k*
FRB 20181122B	0	281.1	85.0	0.98	0.25	14.70	22.00	0.14	4.86	−13.27	729.1	400.2	480.7	0.093	39.36	359.5	0.23	42.22	36.12	*k*
FRB 20181123A	0	300.8	55.9	1.97	0.58	0.99	2.50	1.92	25.60	−64.30	590.2	404.2	488.5	0.697	40.22	315.7	0.34	43.04	36.12	both
FRB 20181125A	0	147.9	33.9	14.75	1.28	0.39	3.20	1.50	9.00	−54.00	533.7	400.2	434.5	0.171	39.02	156.3	1.09	41.17	32.81	both
FRB 20181125A	1	147.9	33.9	14.75	1.44	0.39	3.20	1.50	7.30	−41.80	552.0	400.2	436.6	0.171	39.02	177.8	1.23	41.17	32.81	both
FRB 20181125A	2	147.9	33.9	14.75	1.58	0.39	3.20	1.50	7.30	−58.00	520.9	400.2	426.5	0.171	39.01	141.3	1.35	41.16	32.83	both
FRB 20181126A	0	262.1	81.2	1.97	0.41	3.50	9.40	0.16	17.93	−90.70	518.1	400.2	441.8	0.417	40.29	167.1	0.29	43.01	36.30	both
FRB 20181127A	0	243.8	25.4	3.93	0.74	0.78	2.90	0.58	18.50	−51.30	592.3	400.2	479.3	0.923	40.52	369.4	0.38	43.23	35.68	both
FRB 20181128B	0	157.2	38.3	5.90	1.68	0.34	1.95	0.44	−3.50	−2.20	661.3	400.2	400.2	0.392	39.51	363.6	1.21	41.90	34.37	*k*
FRB 20181128D	0	215.6	59.9	1.97	1.07	2.60	7.00	0.11	−2.48	0.28	800.2	400.2	400.2	0.018	37.36	407.4	1.05	39.94	33.50	*k*
FRB 20181128C	0	268.8	49.7	14.75	2.30	0.39	3.40	2.32	27.40	−75.00	572.1	403.2	480.3	0.557	40.14	263.0	1.48	42.40	33.79	both
FRB 20181128C	1	268.8	49.7	14.75	0.10	0.39	3.40	2.32	23.30	−60.00	590.8	400.2	485.8	0.557	40.15	296.8	0.06	42.40	33.78	both
FRB 20181129B	0	307.6	81.3	1.97	0.36	4.00	9.50	0.83	73.80	−112.00	642.7	482.3	556.8	0.301	40.10	208.7	0.28	42.84	35.87	both
FRB 20181130A	0	355.2	46.5	0.98	0.48	0.97	1.27	0.51	2.70	−45.70	515.9	400.2	412.1	0.033	37.14	119.5	0.46	40.04	34.16	both
FRB 20181203A	0	33.6	23.6	2.95	0.17	1.74	3.60	1.44	13.20	−8.50	800.2	515.2	800.2	0.580	40.43	450.2	0.11	43.31	35.42	both
FRB 20181203B	0	47.3	24.0	3.93	0.58	1.45	4.50	2.32	47.80	−43.60	800.2	550.8	693.2	0.272	39.78	317.2	0.45	42.39	34.54	both
FRB 20181209A	0	98.2	68.7	1.97	0.60	2.50	3.20	0.64	0.42	−25.50	544.7	400.2	403.5	0.206	39.15	174.2	0.50	42.12	35.60	both
FRB 20181213B	0	183.5	53.7	4.92	0.85	0.75	1.70	1.20	45.60	−45.10	800.2	529.6	664.0	0.587	40.03	429.5	0.54	42.88	34.79	both
FRB 20181213C	0	216.4	47.5	2.95	1.25	0.62	1.86	1.50	−2.10	1.20	800.2	400.2	400.2	0.309	39.27	523.5	0.96	41.91	35.01	*k*
FRB 20181214A	0	70.0	43.1	2.95	0.53	0.16	0.41	0.44	23.30	−139.00	494.6	400.2	435.0	0.231	38.39	116.2	0.43	41.06	34.08	both
FRB 20181214F	0	252.6	32.4	8.85	2.30	0.31	2.21	1.52	8.00	−65.00	514.1	400.2	425.7	2.324	41.09	378.6	0.69	43.76	35.42	both
FRB 20181215A	0	93.4	39.3	4.92	1.34	0.34	0.72	1.70	−2.40	−1.10	800.2	400.2	400.2	0.231	38.60	492.4	1.09	41.37	34.05	*k*
FRB 20181216A	0	306.3	53.5	1.97	0.22	0.94	1.70	0.89	14.80	−16.10	800.2	434.2	634.0	0.362	39.58	498.3	0.16	42.45	35.29	*k*
FRB 20181218A	0	5.1	71.3	5.90	1.39	0.83	1.59	0.22	19.00	−83.60	529.3	400.2	448.4	1.894	40.82	373.6	0.48	44.00	36.00	both
FRB 20181218B	0	18.0	69.4	2.95	1.69	0.56	1.80	2.00	−2.70	−2.30	708.8	400.2	400.2	0.573	39.81	485.6	1.07	42.50	35.52	*k*
FRB 20181218C	0	286.0	58.2	4.92	5.20	0.25	1.73	6.80	4.40	−13.10	718.5	400.2	472.7	0.273	39.20	405.3	4.08	41.47	33.92	*k*
FRB 20181219C	0	17.8	14.1	2.95	1.26	0.21	0.57	0.53	−1.00	−4.60	735.5	400.2	400.2	0.605	39.36	538.0	0.79	42.13	35.14	*k*
FRB 20181220A	0	346.1	48.4	2.95	0.43	1.33	3.00	0.46	−5.26	−1.30	596.4	400.2	400.2	0.002	35.16	196.6	0.43	37.81	31.02	both
FRB 20181220B	0	277.4	84.9	1.97	0.56	2.90	3.80	0.62	0.45	−4.80	800.2	400.2	419.5	0.134	38.86	453.7	0.49	41.80	35.25	*k*
FRB 20181221A	0	230.6	25.9	4.92	0.75	1.25	5.80	1.32	62.10	−128.00	583.3	446.1	510.1	0.240	39.65	170.2	0.61	42.07	34.44	both
FRB 20181221B	0	306.3	81.0	2.95	1.04	0.97	3.30	1.10	25.30	−61.20	597.6	405.4	492.2	1.419	40.94	465.0	0.43	43.80	36.36	*k*
FRB 20181222D	0	188.2	56.2	22.61	3.75	0.22	1.23	1.95	8.40	−41.10	561.3	400.2	443.0	1.481	40.51	399.8	1.51	43.15	34.07	both
FRB 20181222E	0	50.6	87.0	3.93	0.25	1.12	5.50	0.79	5.13	−19.90	639.5	400.2	455.2	0.212	39.46	290.0	0.21	41.86	34.57	both
FRB 20181222E	1	50.6	87.0	3.93	0.91	1.12	5.50	0.79	9.90	−23.80	672.3	400.2	492.8	0.212	39.50	329.8	0.75	41.89	34.50	*k*
FRB 20181223B	0	174.9	21.6	8.85	1.57	0.68	4.10	3.50	33.30	−41.00	761.2	473.8	600.6	0.525	40.27	438.2	1.03	42.67	34.22	*k*
FRB 20181223C	0	181.1	27.6	1.97	0.51	1.36	2.84	0.11	2.68	−7.40	800.2	400.2	479.2	0.002	35.21	400.9	0.51	37.89	31.23	*k*
FRB 20181224A	0	355.1	44.6	1.97	0.39	4.30	3.30	0.40	3.85	−6.08	800.2	400.2	549.5	0.160	39.07	464.0	0.33	42.25	35.34	*k*
FRB 20181224E	0	239.3	7.3	1.97	1.06	3.60	10.30	1.10	−1.18	−4.40	729.5	400.2	400.2	0.530	40.50	504.0	0.69	43.23	36.61	*k*
FRB 20181225B	0	36.8	88.2	2.95	1.30	1.90	7.50	1.40	6.80	−10.10	800.2	400.2	560.7	0.179	39.54	471.7	1.10	42.01	34.72	*k*
FRB 20181226C	0	349.1	44.9	3.93	0.63	0.88	2.70	1.98	−1.09	−1.90	800.2	400.2	400.2	0.268	39.31	507.0	0.50	41.92	34.79	*k*
FRB 20181226D	0	120.2	22.2	1.97	0.57	1.89	3.00	0.62	0.44	−5.20	800.2	400.2	417.2	0.274	39.39	509.6	0.45	42.30	35.70	*k*
FRB 20181226B	0	182.7	12.4	1.97	0.59	8.90	52.00	1.10	4.10	−14.40	687.5	400.2	461.1	0.201	40.40	345.2	0.49	42.71	36.01	*k*
FRB 20181226B	1	182.7	12.4	1.97	0.87	8.90	52.00	1.10	1.03	−7.00	764.2	400.2	430.7	0.201	40.37	437.3	0.72	42.68	36.07	*k*
FRB 20181226B	2	182.7	12.4	1.97	1.00	8.90	52.00	1.10	11.50	−18.10	784.9	400.2	549.7	0.201	40.47	462.2	0.84	42.79	35.86	*k*

Table 6
(Continued)

FRB Name	Sub Num	R.A.(J2000) (deg)	Decl. (J2000) (deg)	Δt_{bc} (ms)	Δt_{fitb} (ms)	S_ν (Jy)	F_ν (Jy · ms)	Δt_{sc} (ms)	γ	r	ν_{max} (MHz)	ν_{min} (MHz)	ν_{peak} (MHz)	z	log E (erg)	$\Delta\nu$ (MHz)	Δt_{rw} (ms)	log L (erg s^{-1})	log T_B (K)	Note
FRB 20181226E	0	303.6	73.6	2.95	1.17	0.48	1.35	1.30	−5.80	−3.40	558.3	400.2	400.2	0.178	38.64	186.2	0.99	41.26	34.41	both
FRB 20181228B	0	250.4	63.9	4.92	0.10	0.40	1.67	1.16	59.30	−353.00	471.8	401.5	435.2	0.512	39.72	106.3	0.07	42.28	34.76	both
FRB 20181229B	0	238.4	19.8	20.64	3.36	0.42	4.90	5.10	22.00	−103.00	517.5	400.2	445.5	0.320	39.77	154.8	2.55	41.83	33.09	both
FRB 20181230A	0	346.7	83.4	34.41	1.64	0.94	18.00	41.00	33.00	−27.80	800.2	543.5	724.8	0.704	41.25	437.4	0.96	43.20	33.28	both
FRB 20181231B	0	128.8	56.0	2.95	0.34	0.89	2.34	1.75	59.60	−60.00	800.0	540.6	657.7	0.066	38.22	276.6	0.32	40.82	33.37	both
FRB 20181231C	0	197.1	69.2	1.97	0.39	0.68	1.20	0.41	0.41	−9.60	667.0	400.2	408.8	0.503	39.53	400.9	0.26	42.46	35.82	*k*
FRB 20190101B	0	307.8	29.9	2.95	0.32	1.02	4.40	5.16	41.70	−36.10	800.2	554.3	713.6	1.139	41.05	526.0	0.15	43.74	35.88	both
FRB 20190102A	0	9.3	26.7	3.93	0.82	1.12	4.20	0.99	28.90	−67.80	595.5	411.9	495.2	0.653	40.39	303.6	0.50	43.03	35.51	both
FRB 20190102B	0	21.7	21.4	2.95	0.85	1.71	3.90	0.93	0.60	−4.40	800.2	400.2	428.8	0.281	39.54	512.2	0.66	42.29	35.31	*k*
FRB 20190103B	0	93.6	19.7	31.46	5.83	0.68	12.90	5.40	7.70	−16.30	738.4	400.2	507.0	0.313	40.23	444.1	4.44	42.07	32.81	*k*
FRB 20190106A	0	22.2	46.1	6.88	0.94	0.27	0.81	5.80	9.00	−5.00	800.2	493.5	800.2	0.192	38.79	365.5	0.79	41.38	32.89	both
FRB 20190106B	0	335.6	46.1	1.97	0.58	1.70	3.80	0.60	16.58	−68.00	543.5	400.2	452.1	0.098	38.61	157.3	0.53	41.30	34.67	both
FRB 20190107A	0	0.9	21.8	47.19	25.90	0.49	6.30	20.40	−4.30	−0.40	666.9	400.2	400.2	0.824	40.68	486.5	14.20	42.83	33.38	*k*
FRB 20190107B	0	33.5	83.4	0.98	0.45	2.80	4.30	0.50	−1.30	−3.10	785.3	400.2	400.2	0.002	35.31	386.0	0.45	38.13	32.30	*k*
FRB 20190109A	0	108.0	5.2	13.76	1.65	1.19	6.40	2.20	6.10	−8.10	800.2	400.2	583.0	0.100	38.97	440.0	1.50	41.28	32.63	*k*
FRB 20190109A	1	108.0	5.2	13.76	3.40	1.19	6.40	2.20	4.60	−8.50	800.2	400.2	523.6	0.100	38.92	440.0	3.09	41.23	32.72	*k*
FRB 20190109B	0	253.5	1.2	6.88	0.34	1.20	3.00	0.26	2.50	−65.00	492.4	400.2	408.1	0.009	36.40	93.1	0.34	39.00	31.46	both
FRB 20190110A	0	65.0	47.4	2.95	0.20	1.54	3.80	0.38	6.30	−118.00	472.7	400.2	411.0	0.231	39.34	89.3	0.16	42.03	35.13	both
FRB 20190110C	0	247.0	41.4	2.95	0.39	0.64	1.40	0.22	24.50	−186.00	477.7	400.2	427.4	0.112	38.27	86.2	0.35	40.98	34.06	both
FRB 20190111A	0	217.0	26.8	5.90	0.36	3.60	17.00	0.54	6.35	−6.78	800.2	400.2	638.9	0.066	39.07	426.6	0.34	41.42	33.40	*k*
FRB 20190111A	1	217.0	26.8	5.90	0.44	3.60	17.00	0.54	7.91	−23.30	649.7	400.2	474.4	0.066	38.94	266.1	0.41	41.29	33.66	both
FRB 20190111A	2	217.0	26.8	5.90	0.79	3.60	17.00	0.54	−2.30	−5.80	635.8	400.2	400.2	0.066	38.87	251.2	0.74	41.22	33.81	both
FRB 20190111B	0	260.0	13.5	3.93	0.16	0.32	0.78	0.20	1.90	−17.20	609.1	400.2	422.5	1.348	40.21	490.5	0.07	43.19	35.72	*k*
FRB 20190112A	0	258.0	61.2	9.83	1.64	1.40	16.20	11.01	57.10	−51.40	800.2	564.6	697.7	0.348	40.56	317.5	1.22	42.63	33.95	both
FRB 20190113A	0	108.1	−3.0	6.88	1.82	1.30	5.60	2.20	7.30	−2.80	800.2	491.9	800.2	0.190	39.62	366.9	1.53	42.06	33.56	both
FRB 20190114A	0	8.9	19.2	4.92	1.34	0.55	2.30	0.38	11.10	−89.00	500.0	400.2	425.8	0.869	40.31	186.5	0.72	42.96	35.38	both
FRB 20190116F	0	261.7	75.0	2.95	1.23	0.49	1.54	1.50	3.60	−3.80	800.2	400.2	637.5	0.214	39.07	485.7	1.01	41.65	34.18	*k*
FRB 20190118A	0	253.3	11.6	1.97	0.14	9.30	18.00	0.28	19.42	−56.71	580.9	400.2	474.9	0.093	39.27	197.6	0.13	42.02	35.32	both
FRB 20190122C	2	200.6	17.6	14.75	2.94	4.20	47.00	0.10	4.20	−13.10	714.3	400.2	469.5	0.664	41.43	522.8	1.77	43.60	34.99	*k*
FRB 20190122C	3	200.6	17.6	14.75	8.90	4.20	47.00	0.10	−2.00	−4.00	669.5	400.2	400.2	0.664	41.36	448.2	5.35	43.53	35.13	*k*
FRB 20190122C	5	200.6	17.6	14.75	5.00	4.20	47.00	0.10	−1.40	−4.40	715.1	400.2	400.2	0.664	41.36	524.1	3.00	43.53	35.13	*k*
FRB 20190124C	0	217.2	28.4	13.76	0.29	2.50	13.70	0.67	0.42	−3.54	800.2	400.2	424.6	0.229	39.90	491.5	0.24	42.25	33.96	*k*
FRB 20190124C	1	217.2	28.4	13.76	1.77	2.50	13.70	0.67	1.31	−8.59	724.9	400.2	431.9	0.229	39.90	399.0	1.44	42.26	33.95	*k*
FRB 20190124D	0	237.3	81.2	4.92	0.50	0.50	1.90	0.97	0.10	−9.90	651.0	400.2	402.1	0.243	39.07	311.8	0.40	41.59	34.26	both
FRB 20190124E	0	297.8	20.6	18.68	5.74	0.64	7.30	7.50	9.10	−10.20	800.2	400.2	625.6	0.161	39.48	464.3	4.95	41.48	32.45	*k*
FRB 20190124F	0	338.9	5.3	1.97	0.73	3.90	6.40	0.16	2.05	−16.60	617.4	400.2	425.6	0.150	39.19	249.8	0.64	42.04	35.46	both
FRB 20190125A	0	45.7	27.8	13.76	3.21	0.37	2.60	4.10	36.00	−37.00	800.2	510.1	655.5	0.484	40.04	430.6	2.16	42.36	33.43	both
FRB 20190125B	0	231.4	50.5	6.88	2.47	0.83	4.70	0.95	5.70	−6.80	800.2	400.2	609.9	0.059	38.39	423.7	2.33	40.66	32.57	*k*
FRB 20190128B	0	127.4	23.3	1.97	0.60	0.81	1.64	0.21	5.30	−10.30	800.2	400.2	515.9	0.118	38.47	447.1	0.54	41.21	34.40	*k*
FRB 20190128C	0	69.8	78.9	15.73	6.16	0.71	5.90	7.60	22.60	−55.00	603.2	400.6	491.6	0.177	39.37	238.5	5.23	41.52	32.94	both
FRB 20190128D	0	283.3	17.4	4.92	1.27	1.20	3.60	1.50	0.80	−8.50	705.4	400.2	419.5	0.126	38.78	343.6	1.13	41.35	34.01	*k*
FRB 20190129A	0	45.1	21.4	8.85	1.13	0.49	5.00	10.20	43.00	−37.80	800.2	552.8	707.7	0.404	40.19	347.2	0.81	42.33	33.70	both
FRB 20190130A	0	25.6	13.2	14.75	0.99	0.47	4.40	3.20	19.30	−62.00	567.2	400.2	467.7	1.416	41.05	403.5	0.41	43.46	34.69	both
FRB 20190130B	0	172.1	16.1	3.93	0.27	0.77	2.95	0.77	55.40	−140.80	553.6	428.6	487.1	0.992	40.59	249.0	0.13	43.31	35.72	both
FRB 20190131E	0	195.7	80.9	0.98	0.23	3.00	5.10	0.16	22.00	−63.10	576.8	400.2	476.5	0.174	39.27	207.3	0.20	42.11	35.99	both

Table 6
(Continued)

FRB Name	Sub Num	R.A.(J2000) (deg)	Decl. (J2000) (deg)	Δt_{bc} (ms)	Δt_{fitb} (ms)	S_ν (Jy)	F_ν (Jy · ms)	Δt_{sc} (ms)	γ	r	ν_{max} (MHz)	ν_{min} (MHz)	ν_{peak} (MHz)	z	log E (erg)	$\Delta\nu$ (MHz)	Δt_{rw} (ms)	log L (erg s^{-1})	log T_B (K)	Note
FRB 20190201B	0	118.2	55.6	2.95	0.80	0.81	2.30	0.57	1.80	−14.80	632.1	400.2	425.9	0.697	40.12	393.6	0.47	42.90	35.80	*k*
FRB 20190201A	0	64.0	84.8	0.98	0.61	2.60	3.10	0.72	0.10	−0.20	800.2	400.2	476.6	0.103	38.59	441.4	0.55	41.56	35.46	*k*
FRB 20190202A	0	344.2	17.1	1.97	0.71	41.00	95.00	0.72	5.13	−12.38	757.8	400.2	492.3	0.210	40.73	432.8	0.59	43.44	36.66	*k*
FRB 20190203B	0	130.6	61.9	2.95	0.30	0.49	0.93	0.58	1.50	−8.50	735.7	400.2	437.5	0.520	39.48	510.1	0.20	42.38	35.30	*k*
FRB 20190203A	0	133.7	70.8	3.93	0.55	1.21	4.00	0.83	25.00	−75.00	563.4	400.2	472.9	0.337	39.76	218.2	0.41	42.36	34.99	both
FRB 20190204A	0	161.3	61.5	7.86	1.81	0.24	1.50	0.88	2.40	−28.00	557.9	400.2	418.2	0.382	39.39	217.9	1.31	41.73	33.90	both
FRB 20190205A	0	342.2	83.4	2.95	0.60	0.74	1.70	0.69	18.30	−47.30	605.6	400.2	485.7	0.622	39.95	333.2	0.37	42.80	35.55	both
FRB 20190206B	0	49.8	79.5	19.66	7.10	0.95	9.60	9.00	11.60	−24.60	687.6	400.2	506.4	0.219	39.78	350.3	5.82	41.86	33.04	*k*
FRB 20190206A	0	244.8	9.4	5.90	0.80	1.40	9.10	2.74	38.00	−65.70	644.6	443.2	534.5	0.062	38.66	213.8	0.76	40.87	33.08	both
FRB 20190208B	0	91.0	80.9	0.98	0.10	10.30	14.30	0.12	0.69	−8.02	713.9	400.2	417.9	0.651	40.85	518.0	0.06	43.92	37.82	*k*
FRB 20190208C	0	141.6	83.6	0.98	0.41	1.27	1.74	0.45	18.70	−54.60	583.2	400.2	474.9	0.115	38.43	204.0	0.37	41.35	35.25	both
FRB 20190210B	0	104.2	23.7	2.95	0.40	2.60	5.30	0.36	−2.45	−3.09	696.1	400.2	400.2	0.488	40.14	440.4	0.27	43.00	36.05	*k*
FRB 20190210D	0	307.8	55.5	1.97	0.58	1.37	2.50	0.27	20.70	−24.40	800.2	449.9	611.8	0.151	38.95	403.2	0.50	41.75	34.70	*k*
FRB 20190210E	0	313.6	86.7	1.97	0.96	0.69	1.45	1.10	13.40	−40.50	599.4	400.2	472.2	0.505	39.68	299.8	0.64	42.53	35.71	both
FRB 20190211B	0	299.6	61.4	0.98	0.10	0.30	1.35	0.15	1.40	−7.50	764.9	400.2	440.1	0.099	38.16	400.9	0.09	40.55	34.56	*k*
FRB 20190212B	0	140.0	52.1	2.95	0.23	1.55	3.70	0.50	−2.05	−3.60	702.0	400.2	400.2	0.546	40.08	466.5	0.15	42.89	35.92	*k*
FRB 20190212D	0	178.8	66.7	21.63	1.05	0.42	5.70	15.90	−4.20	−0.30	681.6	400.2	400.2	1.156	40.92	606.6	0.49	43.12	34.28	*k*
FRB 20190214C	0	218.9	19.4	6.88	1.68	1.02	5.20	1.08	4.90	−16.70	671.7	400.2	463.1	0.492	40.20	405.1	1.13	42.67	34.79	*k*
FRB 20190215B	0	335.0	45.3	1.97	0.86	2.20	5.60	0.92	−1.27	−2.09	800.2	400.2	400.2	0.051	38.15	420.3	0.82	40.76	34.31	*k*
FRB 20190218B	0	268.7	17.9	17.69	2.05	0.57	5.90	14.10	46.20	−60.00	715.2	483.4	588.0	0.442	40.26	334.2	1.42	42.41	33.41	both
FRB 20190218C	0	157.0	78.0	0.98	0.21	19.00	31.00	0.11	3.08	−16.09	643.0	400.2	440.4	0.221	40.24	296.4	0.17	43.11	37.07	both
FRB 20190220A	0	237.2	74.2	1.97	0.55	0.34	0.68	0.24	−3.30	−3.30	642.4	400.2	400.2	0.098	37.81	265.9	0.50	40.55	34.08	both
FRB 20190221A	0	132.6	9.9	2.95	0.97	1.23	2.33	0.41	5.10	−23.90	606.5	400.2	444.8	0.092	38.34	225.4	0.89	41.10	34.14	both
FRB 20190221B	0	286.8	27.9	6.88	3.94	0.69	5.60	4.90	−0.30	−2.40	800.2	400.2	400.2	0.163	39.18	465.2	3.39	41.34	33.75	*k*
FRB 20190221D	0	24.8	60.9	1.97	0.77	0.65	1.13	0.95	0.30	−2.40	800.2	400.2	427.2	0.231	38.83	492.5	0.63	41.68	35.07	*k*
FRB 20190222B	0	160.7	19.6	21.63	1.52	0.40	4.40	5.26	−1.80	−10.20	593.5	400.2	400.2	0.439	39.96	278.2	1.06	42.08	33.41	both
FRB 20190222C	0	239.2	40.0	1.97	0.68	0.44	0.83	0.74	9.30	−53.90	536.4	400.2	436.3	0.473	39.34	200.7	0.46	42.24	35.52	both
FRB 20190223A	0	64.7	87.7	3.93	0.76	0.47	1.58	0.87	21.80	−103.00	516.5	400.2	444.8	0.286	39.18	149.6	0.59	41.76	34.49	both
FRB 20190224A	0	60.5	83.4	16.71	2.04	0.63	8.50	5.77	2.60	−60.00	497.5	400.2	408.9	0.762	40.75	171.4	1.16	42.86	34.30	both
FRB 20190224E	0	183.0	61.5	1.97	0.55	2.03	4.00	0.57	2.22	−8.64	762.2	400.2	454.9	0.369	39.82	495.7	0.40	42.67	35.93	*k*
FRB 20190226B	0	273.6	61.8	18.68	4.00	0.38	2.38	4.90	29.90	−39.30	745.3	459.4	585.2	0.570	40.10	448.9	2.55	42.49	33.42	*k*
FRB 20190226C	0	17.5	26.8	4.92	1.31	0.39	1.41	1.50	6.60	−42.00	548.3	400.2	433.3	0.795	40.03	265.9	0.73	42.73	35.14	both
FRB 20190227B	0	220.5	39.8	0.98	0.40	0.48	0.71	0.47	−0.50	−0.80	800.2	400.2	400.2	0.259	38.70	503.4	0.32	41.63	35.70	*k*
FRB 20190228A	0	183.5	22.9	30.47	2.25	1.79	35.80	18.91	52.60	−51.90	800.2	538.4	664.7	0.365	40.93	357.3	1.65	42.76	33.16	both
FRB 20190301B	0	69.5	74.1	3.93	1.32	0.40	0.85	1.60	−1.50	−13.40	575.5	400.2	400.2	0.523	39.41	267.0	0.87	42.26	35.05	both
FRB 20190301D	0	278.7	74.7	5.90	0.36	0.39	1.50	0.54	3.60	−29.40	562.7	400.2	425.4	1.159	40.37	350.9	0.17	43.12	35.32	both
FRB 20190303B	0	128.7	66.0	4.92	0.72	9.40	42.00	1.57	−1.68	−2.56	786.7	400.2	400.2	0.061	39.19	410.1	0.67	41.56	34.31	*k*
FRB 20190303D	0	179.6	70.8	2.95	0.81	0.59	1.17	1.00	−0.90	−5.60	704.3	400.2	400.2	0.674	39.77	509.1	0.48	42.70	35.69	*k*
FRB 20190304A	0	124.5	74.6	2.95	0.41	0.71	2.90	0.90	6.30	−67.30	504.7	400.2	419.4	0.405	39.73	146.8	0.29	42.27	35.28	both
FRB 20190304B	0	204.9	24.2	2.95	0.33	0.67	2.22	0.62	−1.24	−7.40	646.5	400.2	400.2	0.420	39.63	349.8	0.23	42.26	35.32	*k*
FRB 20190304C	0	223.0	26.7	2.95	0.95	0.53	1.32	1.10	22.30	−87.00	535.2	400.2	454.9	0.528	39.66	206.2	0.62	42.45	35.32	both
FRB 20190308C	0	188.4	44.4	21.63	0.40	0.47	4.80	2.29	15.20	−61.00	550.7	400.2	453.4	0.454	40.09	218.9	0.28	42.24	33.40	both
FRB 20190308C	1	188.4	44.4	21.63	0.55	0.47	4.80	2.29	13.90	−60.50	545.7	400.2	449.0	0.454	40.08	211.6	0.38	42.24	33.41	both
FRB 20190308B	0	38.6	83.6	1.97	0.19	1.11	1.39	0.13	18.60	−52.90	587.9	400.2	477.2	0.015	36.57	190.6	0.18	39.48	32.82	both
FRB 20190308B	1	38.6	83.6	1.97	0.52	1.11	1.39	0.13	9.50	−37.00	585.3	400.2	455.5	0.015	36.55	187.9	0.51	39.46	32.86	both

Table 6
(Continued)

FRB Name	Sub Num	R.A.(J2000) (deg)	Decl. (J2000) (deg)	Δt_{bc} (ms)	Δt_{fitb} (ms)	S_ν (Jy)	F_ν (Jy · ms)	Δt_{sc} (ms)	γ	r	ν_{max} (MHz)	ν_{min} (MHz)	ν_{peak} (MHz)	z	log E (erg)	$\Delta\nu$ (MHz)	Δt_{rw} (ms)	log L (erg s^{-1})	log T_B (K)	Note
FRB 20190309A	0	279.0	52.4	1.97	0.58	0.39	0.72	0.75	12.90	−64.00	535.8	400.2	442.9	0.248	38.71	169.2	0.47	41.54	34.88	both
FRB 20190318A	0	324.1	74.5	12.78	0.93	1.55	14.20	6.23	0.04	−3.04	800.2	400.2	402.9	0.290	40.10	515.9	0.72	42.25	34.08	*k*
FRB 20190320C	0	254.7	22.4	3.93	1.04	1.24	3.14	1.30	0.40	−2.20	800.2	400.2	442.0	0.275	39.44	510.2	0.82	42.14	34.88	*k*
FRB 20190320E	0	76.6	89.2	2.95	0.83	4.40	12.30	0.72	6.06	−7.70	800.2	400.2	592.6	0.182	39.79	472.8	0.70	42.42	35.05	*k*
FRB 20190322B	0	132.0	73.3	2.95	1.30	0.61	2.04	1.70	−0.10	−6.20	725.7	400.2	400.2	0.513	39.77	492.6	0.86	42.43	35.46	*k*
FRB 20190323C	0	199.5	40.1	2.95	0.31	0.56	1.38	1.08	2.70	−10.70	722.5	400.2	454.3	0.317	39.22	424.5	0.24	41.95	34.88	*k*
FRB 20190323D	0	56.9	46.9	12.78	5.43	0.37	2.49	7.00	−7.50	−3.00	528.8	400.2	400.2	0.593	39.99	204.9	3.41	42.36	34.10	both
FRB 20190325A	0	130.4	83.1	2.95	1.56	1.31	4.60	1.80	−0.80	−1.20	800.2	400.2	400.2	0.260	39.51	503.9	1.24	42.07	35.18	*k*
FRB 20190326A	0	161.9	74.2	0.98	0.46	1.02	1.51	0.55	2.10	−7.70	791.7	400.2	458.0	0.181	38.76	462.4	0.39	41.67	35.59	*k*
FRB 20190327A	0	281.3	34.3	1.97	0.30	2.43	5.20	0.33	−0.79	−2.15	800.2	400.2	400.2	0.200	39.33	479.8	0.25	42.08	35.57	*k*
FRB 20190329A	0	65.5	73.6	11.80	1.04	0.52	2.24	0.90	42.00	−272.00	473.9	400.2	432.3	0.001	34.42	73.8	1.04	36.79	28.70	both
FRB 20190402A	0	178.6	47.1	15.73	5.33	0.30	1.34	6.60	4.10	−16.70	657.4	400.2	453.3	1.340	40.47	602.0	2.28	43.19	34.42	*k*
FRB 20190403G	0	81.7	25.8	1.97	1.59	0.75	1.59	1.90	35.70	−76.00	603.2	425.5	506.6	0.703	40.04	302.6	0.93	42.95	35.98	both
FRB 20190403B	0	135.5	1.5	10.81	2.35	2.70	23.80	5.78	2.80	−11.10	714.3	400.2	453.2	0.176	39.93	369.4	2.00	42.06	33.91	*k*
FRB 20190403C	0	249.8	58.7	4.92	0.87	0.37	1.53	1.86	−1.30	−6.70	659.0	400.2	400.2	0.921	40.16	497.1	0.45	42.83	35.32	*k*
FRB 20190403D	0	326.5	84.3	2.95	1.31	0.65	1.75	1.70	−2.40	−3.10	700.9	400.2	400.2	0.536	39.74	462.0	0.85	42.50	35.53	*k*
FRB 20190403E	0	220.2	86.5	18.68	2.20	3.90	76.00	18.20	31.70	−36.20	798.7	482.1	620.6	0.099	40.06	348.0	2.00	41.81	32.81	both
FRB 20190404B	0	259.8	40.0	0.98	0.33	8.60	16.30	0.11	−2.29	−2.66	725.3	400.2	400.2	0.417	40.49	460.6	0.23	43.36	37.38	*k*
FRB 20190405A	0	337.0	21.0	13.76	1.11	0.65	2.50	2.49	3.30	−11.70	716.7	400.2	460.0	0.340	39.55	424.2	0.83	42.09	33.66	*k*
FRB 20190408A	0	262.2	71.6	1.97	0.84	0.64	1.51	1.00	35.70	−49.00	716.5	464.1	576.6	0.833	40.23	462.7	0.46	43.12	35.94	*k*
FRB 20190409B	0	126.7	63.5	30.47	2.34	0.39	6.80	20.90	21.10	−34.10	707.3	420.6	545.5	0.175	39.46	337.0	1.99	41.29	32.01	*k*
FRB 20190410A	0	263.5	−2.4	6.88	1.01	1.59	5.80	1.20	43.00	−85.00	607.9	437.4	515.7	0.073	38.59	182.9	0.94	41.06	33.18	both
FRB 20190410B	0	265.8	15.2	1.97	0.42	0.22	0.45	0.21	18.70	−73.40	542.5	400.2	454.4	0.551	39.23	220.7	0.27	42.11	35.32	both
FRB 20190411C	0	9.3	20.5	2.95	1.02	3.19	9.30	1.10	24.30	−26.10	800.2	473.1	636.5	0.122	39.35	367.2	0.91	41.93	34.49	both
FRB 20190411C	1	9.3	20.5	2.95	0.89	3.19	9.30	1.10	11.70	−12.50	800.2	416.6	640.1	0.122	39.35	430.6	0.79	41.93	34.49	*k*
FRB 20190412B	0	285.6	19.2	42.27	6.80	0.68	12.80	15.50	−4.00	−2.70	625.5	400.2	400.2	0.015	37.42	228.6	6.70	39.15	30.05	both
FRB 20190414A	0	181.4	38.9	4.92	1.95	0.44	1.74	2.40	−3.40	−0.70	728.1	400.2	400.2	0.805	40.10	591.8	1.08	42.76	35.27	*k*
FRB 20190415C	0	74.8	34.8	4.92	0.55	0.46	0.77	0.87	13.40	−32.00	648.9	400.2	495.3	0.459	39.34	362.9	0.38	42.28	34.61	*k*
FRB 20190416B	0	172.2	36.0	5.90	0.79	0.69	1.47	0.49	−3.60	−23.50	511.9	400.2	400.2	0.541	39.67	172.1	0.51	42.53	34.96	both
FRB 20190417C	0	45.7	71.3	0.98	0.41	7.90	10.80	0.43	24.78	−32.41	765.8	449.3	586.6	0.127	39.41	356.6	0.37	42.32	35.95	both
FRB 20190418A	0	65.8	16.0	1.97	0.71	0.99	2.20	0.78	−4.80	−3.70	579.7	400.2	400.2	0.019	36.89	183.0	0.69	39.55	33.11	both
FRB 20190419A	0	105.0	64.9	3.93	1.85	0.41	0.77	2.40	1.00	−29.00	538.6	400.2	407.1	0.341	38.99	185.5	1.38	41.84	34.66	both
FRB 20190419B	0	255.3	86.7	1.97	0.66	4.60	7.90	0.25	5.65	−14.30	728.4	400.2	487.6	0.017	37.43	333.8	0.64	40.20	33.51	*k*
FRB 20190420A	0	106.5	56.0	1.97	0.77	0.88	3.11	2.64	11.50	−6.10	800.2	528.7	800.2	0.528	40.28	414.9	0.50	42.92	35.40	both
FRB 20190420C	0	248.1	37.2	13.76	1.95	0.44	4.13	8.00	−0.50	−6.40	700.0	400.2	400.2	0.585	40.19	475.2	1.23	42.42	34.10	*k*
FRB 20190421B	0	82.5	62.3	2.95	1.12	5.10	16.40	1.20	−0.13	−0.80	800.2	400.2	400.2	0.245	40.01	498.0	0.90	42.60	35.72	*k*
FRB 20190422A	0	48.6	35.1	29.49	3.22	0.60	9.10	2.70	42.00	−46.90	781.4	501.7	626.1	0.335	40.23	373.4	2.41	42.18	32.68	both
FRB 20190422A	1	48.6	35.1	29.49	2.31	0.60	9.10	2.70	54.20	−63.70	740.5	506.3	612.3	0.335	40.22	312.6	1.73	42.17	32.70	both
FRB 20190422A	2	48.6	35.1	29.49	2.00	0.60	9.10	2.70	24.00	−32.00	763.7	444.8	582.8	0.335	40.20	425.7	1.50	42.14	32.75	*k*
FRB 20190423A	0	179.7	55.2	5.90	0.41	10.80	55.40	0.54	11.19	−30.52	632.6	400.2	480.7	0.143	40.14	265.5	0.36	42.48	34.80	both
FRB 20190423A	1	179.7	55.2	5.90	2.37	10.80	55.40	0.54	−3.66	−5.59	593.0	400.2	400.2	0.143	40.06	220.3	2.07	42.40	34.96	both
FRB 20190423B	0	298.6	26.2	9.83	2.49	0.87	7.00	3.00	62.40	−106.00	623.1	463.8	537.6	0.003	35.93	159.8	2.48	38.03	29.81	both
FRB 20190423B	1	298.6	26.2	9.83	8.50	0.87	7.00	3.00	63.00	−116.00	604.1	455.6	524.6	0.003	35.92	149.0	8.47	38.02	29.83	both
FRB 20190423C	0	349.1	87.0	7.86	0.16	1.23	4.37	2.48	1.90	−12.30	668.0	400.2	433.0	0.808	40.54	484.3	0.09	43.24	35.25	*k*
FRB 20190425A	0	255.7	21.5	0.98	0.38	18.60	31.60	0.38	8.26	−10.56	800.2	400.2	591.8	0.002	36.35	400.9	0.38	39.12	32.78	*k*

Table 6
(Continued)

FRB Name	Sub Num	R.A.(J2000) (deg)	Decl. (J2000) (deg)	Δt_{bc} (ms)	Δt_{fitb} (ms)	S_ν (Jy)	F_ν (Jy · ms)	Δt_{sc} (ms)	γ	r	ν_{max} (MHz)	ν_{min} (MHz)	ν_{peak} (MHz)	z	log E (erg)	$\Delta\nu$ (MHz)	Δt_{rw} (ms)	log L (erg s^{-1})	log T_B (K)	Note
FRB 20190425B	0	210.1	88.6	1.97	1.11	1.25	3.10	1.30	22.40	−65.60	572.6	400.2	474.8	1.014	40.62	347.2	0.55	43.53	36.57	both
FRB 20190426A	0	115.0	59.1	1.97	0.40	1.59	2.01	0.43	27.00	−71.70	577.8	403.7	483.0	0.232	39.13	214.5	0.32	42.12	35.35	both
FRB 20190427A	0	78.9	7.8	1.97	0.34	3.90	9.50	0.65	−2.62	3.30	800.2	400.2	400.2	0.333	40.05	533.0	0.25	42.79	36.23	*k*
FRB 20190428A	0	170.7	23.3	3.93	0.37	2.22	7.40	3.63	54.00	−48.80	800.2	560.1	696.0	0.973	41.13	473.7	0.19	43.90	35.85	both
FRB 20190429B	0	329.9	4.0	16.71	6.38	0.74	5.00	7.80	99.00	−910.00	444.1	401.7	422.4	0.194	39.31	50.6	5.34	41.56	33.12	both
FRB 20190430A	0	77.7	87.0	19.66	3.38	0.75	7.70	3.23	4.70	−29.10	574.6	400.2	433.8	0.228	39.65	214.1	2.75	41.73	33.11	both
FRB 20190430C	0	277.2	24.9	2.95	0.89	2.17	5.10	1.10	48.70	−48.80	800.2	530.6	659.3	0.252	39.75	337.5	0.71	42.47	34.94	both
FRB 20190501B	0	261.4	54.4	5.90	0.93	0.88	3.20	1.10	−0.03	−6.80	714.8	400.2	400.2	0.748	40.30	549.8	0.53	42.98	35.35	*k*
FRB 20190502C	0	155.6	83.0	1.97	0.53	3.60	8.30	0.32	9.00	−26.80	634.3	400.2	473.2	0.308	39.99	306.2	0.40	42.75	35.98	both
FRB 20190515B	0	0.8	3.4	4.92	0.38	2.80	11.30	1.88	0.77	−9.30	685.6	400.2	417.0	0.802	40.93	514.4	0.21	43.58	36.04	*k*
FRB 20190515D	0	67.1	−5.0	4.92	0.42	3.00	8.80	1.49	30.60	−54.30	651.5	431.6	530.2	0.341	40.16	294.9	0.31	42.82	35.10	both
FRB 20190516B	0	167.3	7.4	13.76	1.49	1.13	9.90	3.72	1.10	−12.20	647.1	400.2	419.4	1.267	41.26	559.8	0.66	43.67	35.14	*k*
FRB 20190517C	0	87.5	26.6	1.97	0.38	3.10	8.70	0.15	8.48	−50.20	539.4	400.2	435.5	0.063	38.56	147.9	0.35	41.14	34.57	both
FRB 20190518C	0	242.0	4.6	2.95	0.64	6.70	14.80	0.29	6.39	−15.10	730.2	400.2	494.3	0.369	40.43	451.7	0.46	43.22	36.02	*k*
FRB 20190518D	0	174.7	89.3	1.97	0.26	1.36	3.00	0.39	5.40	−15.60	698.5	400.2	475.6	0.064	38.15	317.3	0.24	40.84	34.15	*k*
FRB 20190518G	0	94.8	75.5	0.98	0.67	0.99	1.76	0.72	19.80	−75.30	543.6	400.2	456.4	0.437	39.62	206.0	0.46	42.53	36.37	both
FRB 20190519E	0	168.3	41.6	0.98	0.41	1.00	1.46	0.45	2.00	4.10	800.2	551.0	800.2	0.665	40.16	415.0	0.25	43.21	36.26	both
FRB 20190519F	0	165.6	77.2	6.88	1.36	0.75	4.00	1.36	21.70	−86.40	534.4	400.2	453.9	0.765	40.47	236.8	0.77	42.99	35.06	both
FRB 20190519H	0	343.0	87.4	2.95	0.25	3.20	6.60	0.31	2.33	−14.00	652.9	400.2	435.0	1.164	41.03	546.8	0.12	44.05	36.82	*k*
FRB 20190519J	0	296.2	86.9	1.97	0.46	0.63	1.70	0.50	24.30	−259.00	461.0	400.2	419.5	0.577	39.82	95.9	0.29	42.58	35.89	both
FRB 20190520A	0	273.5	26.3	1.97	0.65	1.08	2.40	0.71	11.40	−54.30	546.0	400.2	444.4	0.312	39.44	191.3	0.49	42.21	35.52	both
FRB 20190527A	0	12.4	8.0	57.02	2.67	0.47	10.10	5.08	47.00	−122.00	556.1	422.4	484.7	0.537	40.59	205.5	1.74	42.44	32.65	both
FRB 20190527A	1	12.4	8.0	57.02	2.47	0.47	10.10	5.08	30.70	−133.00	512.2	400.2	449.1	0.537	40.55	172.1	1.61	42.41	32.72	both
FRB 20190529A	0	68.1	40.3	3.93	1.04	0.47	1.45	1.50	24.20	−97.00	528.9	400.2	453.4	0.523	39.69	196.1	0.68	42.39	35.01	both
FRB 20190530A	0	68.7	60.6	1.97	1.02	0.58	1.69	1.30	17.70	−91.00	517.3	400.2	441.1	0.385	39.47	162.1	0.74	42.15	35.45	both
FRB 20190531C	0	331.1	43.0	2.95	1.45	0.37	1.20	1.90	18.30	−74.00	540.6	400.2	453.0	0.304	39.12	183.0	1.11	41.73	34.67	both
FRB 20190531E	0	15.2	0.5	0.98	0.47	2.70	5.30	0.56	1.10	4.60	800.2	527.0	800.2	0.245	39.82	340.2	0.37	42.63	35.80	both
FRB 20190601B	0	17.9	23.8	24.58	4.04	1.00	13.00	5.67	9.70	−68.60	515.9	400.2	429.5	0.754	40.94	202.9	2.30	43.07	34.11	both
FRB 20190601C	0	88.5	28.5	5.90	0.68	1.32	5.80	0.12	35.30	−68.80	620.8	430.6	517.0	0.175	39.37	223.5	0.58	41.80	34.01	both
FRB 20190601C	1	88.5	28.5	5.90	0.51	1.32	5.80	0.12	36.10	−79.50	595.4	423.6	502.2	0.175	39.36	201.9	0.43	41.79	34.03	both
FRB 20190603B	0	48.9	74.3	3.93	1.54	1.70	6.20	1.90	−0.20	−6.80	706.1	400.2	400.2	0.371	39.96	419.3	1.12	42.54	35.37	*k*
FRB 20190604C	0	77.4	49.3	20.64	5.41	1.56	26.20	11.00	2.56	−10.59	719.8	400.2	451.6	0.310	40.48	418.8	4.13	42.37	33.62	*k*
FRB 20190604G	0	120.8	59.5	4.92	1.19	1.15	4.49	0.31	−2.52	−0.50	800.2	400.2	400.2	0.106	38.70	442.4	1.08	41.15	33.88	*k*
FRB 20190605C	0	168.3	−5.2	0.98	0.49	4.60	4.40	0.52	9.90	−40.50	573.9	400.2	452.2	0.066	38.32	185.1	0.46	41.37	35.35	both
FRB 20190606B	0	108.8	86.8	6.88	1.01	2.62	17.40	4.81	12.40	−17.50	800.2	400.2	569.2	0.157	39.79	462.6	0.87	42.03	33.99	*k*
FRB 20190609A	0	345.3	87.9	4.92	0.43	3.60	10.40	0.50	62.40	−84.00	683.4	491.0	579.3	0.200	39.79	230.9	0.36	42.41	34.62	*k*
FRB 20190609A	1	345.3	87.9	4.92	2.12	3.60	10.40	0.50	55.00	−67.00	722.4	499.1	600.5	0.200	39.81	268.0	1.77	42.43	34.59	*k*
FRB 20190609B	0	210.5	88.3	0.98	0.55	11.50	22.20	0.57	4.11	−10.46	778.7	400.2	487.1	0.178	39.94	445.8	0.47	42.73	36.57	*k*
FRB 20190609C	0	73.2	24.1	0.98	2.07	0.64	1.91	2.60	15.20	−138.00	481.3	400.2	422.9	0.329	39.37	107.8	1.56	42.01	35.99	both
FRB 20190609D	0	115.9	51.7	2.95	1.58	0.66	2.36	2.00	−1.60	−17.00	552.6	400.2	400.2	0.428	39.67	217.6	1.11	42.27	35.33	both
FRB 20190612B	0	222.2	4.3	0.98	0.19	2.41	3.78	0.12	10.60	−25.90	662.1	400.2	491.3	0.078	38.45	282.4	0.17	41.29	35.16	both
FRB 20190613B	0	65.8	42.7	0.98	0.43	1.08	1.26	0.45	2.52	−8.22	792.2	400.2	466.6	0.022	36.82	400.5	0.42	39.77	33.73	*k*
FRB 20190614A	0	179.8	88.3	3.93	1.30	0.83	2.21	0.77	1.60	−29.00	544.0	400.2	411.1	1.051	40.44	294.9	0.63	43.33	35.95	both
FRB 20190616A	0	234.0	34.5	1.97	0.65	0.73	1.67	0.79	−0.80	−1.80	800.2	400.2	400.2	0.113	38.33	445.1	0.59	41.01	34.54	*k*
FRB 20190617A	0	178.6	83.9	4.92	1.49	5.80	21.00	1.50	0.45	−9.35	673.2	400.2	409.9	0.065	38.94	290.6	1.40	41.41	34.13	both

Table 6
(Continued)

FRB Name	Sub Num	R.A.(*J*2000) (deg)	Decl. (*J*2000) (deg)	Δt_{bc} (ms)	Δt_{fitb} (ms)	S_ν (Jy)	F_ν (Jy · ms)	Δt_{sc} (ms)	γ	r	ν_{max} (MHz)	ν_{min} (MHz)	ν_{peak} (MHz)	z	log E (erg)	$\Delta\nu$ (MHz)	Δt_{rw} (ms)	log L (erg s^{-1})	log T_B (K)	Note
FRB 20190617B	0	56.4	1.2	13.76	7.58	0.99	9.20	9.50	10.60	−38.40	586.7	400.2	459.3	0.166	39.47	217.4	6.50	41.57	33.20	both
FRB 20190618A	0	321.2	25.4	1.97	0.55	2.40	4.30	0.58	3.34	−35.80	540.4	400.2	419.3	0.068	38.31	149.7	0.51	41.08	34.56	both
FRB 20190619B	0	231.7	82.2	0.98	0.52	1.96	4.50	0.59	−0.50	−5.60	731.8	400.2	400.2	0.159	39.06	384.5	0.45	41.77	35.88	*k*
FRB 20190619D	0	114.8	41.6	32.44	1.39	0.48	6.50	12.00	−6.46	4.90	800.2	400.2	400.2	0.267	39.69	506.8	1.10	41.66	32.69	*k*
FRB 20190621B	0	193.1	55.6	1.97	1.38	0.30	1.19	1.80	−0.50	−7.70	670.9	400.2	400.2	1.072	40.18	560.9	0.67	42.90	36.15	*k*
FRB 20190621C	0	206.6	5.2	0.98	0.44	1.98	2.38	0.51	39.10	−101.00	564.4	417.5	485.4	0.530	39.95	224.7	0.29	43.05	36.79	both
FRB 20190621D	0	270.6	78.9	3.93	2.29	0.89	4.30	2.60	7.40	−22.30	651.1	400.2	472.1	0.588	40.29	398.4	1.44	42.80	35.36	*k*
FRB 20190622A	0	299.0	85.8	1.97	1.19	0.61	1.28	1.40	0.90	−15.60	605.0	400.2	411.9	1.112	40.25	432.6	0.56	43.26	36.46	*k*
FRB 20190624A	0	168.3	69.8	5.90	1.52	0.58	3.01	0.95	−5.30	2.20	704.0	400.2	400.2	0.966	40.49	597.2	0.77	43.07	35.39	*k*
FRB 20190624B	0	304.6	73.6	0.98	0.37	16.50	20.00	0.40	34.80	−43.20	754.3	475.4	598.8	0.058	39.00	295.2	0.35	41.94	35.56	both
FRB 20190625A	0	227.9	32.9	58.00	3.92	0.35	11.90	16.90	−1.10	−8.10	639.7	400.2	400.2	0.225	39.80	293.4	3.20	41.35	31.89	both
FRB 20190625C	0	73.2	11.1	0.98	0.55	2.22	4.02	0.63	0.30	−5.90	768.7	400.2	410.7	0.327	39.67	489.1	0.41	42.54	36.55	*k*
FRB 20190625D	0	115.0	4.9	1.97	0.69	5.30	12.10	0.72	17.84	−76.10	535.5	400.2	450.0	0.610	40.75	217.8	0.43	43.60	36.80	both
FRB 20190627A	0	195.9	0.8	1.97	0.66	1.98	2.62	0.80	9.30	−27.30	634.6	400.2	474.6	0.336	39.57	313.2	0.50	42.58	35.80	both
FRB 20190628B	0	248.5	80.1	2.95	0.27	0.75	1.39	0.47	−6.00	−0.40	583.5	400.2	400.2	0.322	39.18	242.3	0.20	42.04	35.13	both
FRB 20190629A	0	6.3	12.7	3.93	1.14	0.82	3.05	1.70	24.70	−35.30	733.6	440.1	568.2	0.444	39.97	423.9	0.79	42.56	34.91	*k*
FRB 20190630D	0	143.4	8.9	1.97	0.56	1.73	2.60	0.63	−2.30	−1.60	780.6	400.2	400.2	0.226	39.14	466.3	0.45	42.05	35.53	*k*
FRB 20190701C	0	96.4	81.6	1.97	1.44	0.88	2.50	1.80	46.20	−211.00	495.5	402.2	446.4	0.943	40.44	181.3	0.74	43.27	36.41	both
FRB 20190701D	0	112.1	66.7	8.85	1.40	1.33	8.60	1.53	6.49	−20.90	651.8	400.2	467.6	0.900	40.96	478.1	0.74	43.42	35.21	*k*
FRB 20190609C	0	73.3	24.1	3.93	2.07	0.64	1.91	4.10	15.20	−138.00	481.3	400.2	422.9	0.328	39.36	61.1	1.56	42.01	35.34	both
FRB 20190226B	0	273.6	61.7	10.81	4.00	0.38	2.38	8.00	29.90	−39.30	706.4	474.3	578.8	0.570	40.09	147.8	2.55	42.49	34.77	both
FRB 20190430C	0	277.2	24.8	2.95	0.89	5.80	15.20	1.80	48.70	−48.80	800.2	527.8	655.2	0.251	40.21	217.7	0.71	42.89	36.41	both
FRB 20190110C	0	249.3	41.4	2.95	0.75	0.64	1.40	1.50	28.20	−202.00	477.7	400.2	427.4	0.110	38.26	69.8	0.68	40.96	35.24	both
FRB 20190113A	0	108.3	−3.0	6.88	1.82	1.10	5.70	3.60	7.30	−2.80	800.2	491.9	800.2	0.191	39.63	258.8	1.53	41.99	34.65	both
FRB 20180910A	0	354.8	89.0	0.98	0.21	6.50	5.60	0.24	0.05	−0.53	800.2	400.2	417.6	0.623	40.40	246.4	0.13	43.67	38.94	*k*
FRB 20190303D	0	185.3	70.7	2.95	0.81	0.59	1.17	1.60	−0.90	−5.60	564.8	400.2	440.8	0.674	39.81	98.3	0.48	42.74	36.73	both
FRB 20190328C	0	75.6	82.1	3.93	0.77	4.70	14.90	2.30	0.70	−2.70	800.2	400.2	459.0	0.376	40.41	290.6	0.56	43.05	37.12	*k*
FRB 20190107B	0	49.3	83.4	0.98	0.45	2.80	4.30	0.90	−1.30	−3.10	784.4	400.2	400.2	0.002	35.31	383.3	0.45	38.13	32.98	*k*
FRB 20190210C	0	313.9	89.2	1.97	0.29	2.37	3.60	0.25	0.35	−1.50	800.2	400.2	448.5	0.580	40.17	253.2	0.18	43.19	38.09	*k*
FRB 20190127B	0	169.3	83.5	67.83	2.50	0.63	11.40	42.80	5.30	−7.70	800.2	400.2	562.2	0.609	40.82	248.6	1.55	42.77	35.48	both
FRB 20180909A	0	120.0	57.0	15.73	6.31	0.43	0.90	13.00	−0.30	−1.30	800.2	400.2	400.2	0.316	38.98	304.0	4.80	41.78	34.21	*k*
FRB 20190201A	0	95.9	83.8	0.98	0.61	2.60	3.10	1.20	0.10	−0.20	789.0	400.2	464.9	0.109	38.63	350.5	0.55	41.60	35.95	*k*
FRB 20190308B	0	49.3	83.4	1.97	0.19	1.11	1.39	0.13	18.60	−52.90	587.9	400.2	477.2	0.016	36.63	184.7	0.18	39.54	34.92	both
FRB 20190308B	1	49.3	83.4	1.97	0.52	1.11	1.39	0.13	9.50	−37.00	585.3	400.2	455.5	0.016	36.61	182.1	0.51	39.52	34.07	both

ORCID iDs

Sheng Yang https://orcid.org/0000-0002-2898-6532

References

Adámek, K., & Armour, W. 2020, ApJS, 247, 56
Agarwal, D., Aggarwal, K., Burke-Spolaor, S., Lorimer, D. R., & Garver-Daniels, N. 2020, MNRAS, 497, 1661
Bhardwaj, M., Michilli, D., Kirichenko, A. Y., et al. 2024, ApJL, 971, L51
Bhatporia, S., Walters, A., Murugan, J., & Weltman, A. 2023, arXiv:2311.03456
Breiman, L. 2001, Mach. Learn., 45, 5
Burke-Spolaor, S., & Bannister, K. W. 2014, ApJ, 792, 19
Campello, R. J. G. B., Moulavi, D., & Sander, J. 2013, in Advances in Knowledge Discovery and Data Mining, ed. J. Pei et al. (Berlin: Springer), 160
Campello, R. J. G. B., Moulavi, D., Zimek, A., & Sander, J. 2015, ACM Trans. Knowl. Discov. Data, 10, 5
Chang, C.-C., & Lin, C.-J. 2011, ACM Trans. Intell. Syst. Technol., 2, 27
Chen, B. H., Hashimoto, T., Goto, T., et al. 2021, MNRAS, 509, 1227
Chen, B. H., Hashimoto, T., Goto, T., et al. 2022, MNRAS, 509, 1227
Chen, B. H., Hashimoto, T., Goto, T., et al. 2023, MNRAS, 521, 5738
CHIME/FRB Collaboration, Amiri, M., Bandura, K., et al. 2018, ApJ, 863, 48
CHIME/FRB Collaboration, Amiri, M., Andersen, B. C., et al. 2021, ApJS, 257, 59
CHIME/FRB Collaboration, Andersen, B. C., Bandura, K., et al. 2023, ApJ, 947, 83
Chow, G. C. 1960, Econometrica, 28, 591
Cordes, J. M., & Lazio, T. J. W. 2002, arXiv:astro-ph/0207156
Cover, T., & Hart, P. 1967, ITIT, 13, 21
Dempster, A. P., Laird, N. M., & Rubin, D. B. 2018, Journal of the Royal Statistical Society: Series B (Methodological), 39, 1
Deng, W., & Zhang, B. 2014, ApJL, 783, L35
Ester, M., Kriegel, H.-P., Sander, J., Xu, X., et al. 1996, in Proc. of the Second Int. Conf. on Knowledge Discovery and Data Mining, ed. E. Simoudis, J. Han, & U. Fayyad (Palo Alto, CA: AAAI Press), 226
Fonseca, E., Andersen, B. C., Bhardwaj, M., et al. 2020, ApJL, 891, L6
Fotopoulou, S. 2024, A&C, 48, 100851
Gao, H., Li, Z., & Zhang, B. 2014, ApJ, 788, 189
Gordon, A. C., Fong, W.-f., Kilpatrick, C. D., et al. 2023, ApJ, 954, 80
Guo, H.-Y., & Wei, H. 2022, JCAP, 07, 010
Guo, H.-Y., & Wei, H. 2024, PhLB, 859, 139120
Hallinan, G., Ravi, V., Weinreb, S., et al. 2019, BAAS, 51, 255
Han, J., Kamber, M., & Pei, J. 2012, in Data Mining, ed. J. Han, M. Kamber, & J. Pei (3rd ed.; San Mateo, CA: Morgan Kaufmann Publishers), 443
Kocz, J., Ravi, V., Catha, M., et al. 2019, MNRAS, 489, 919
Jankowski, F., Bezuidenhout, M. C., Caleb, M., et al. 2023, MNRAS, 524, 4275
Keane, E. F. 2018, NatAs, 2, 865
Kirsten, F., Marcote, B., Nimmo, K., et al. 2022, Natur, 602, 585
Kumar, P., Shannon, R. M., Osłowski, S., et al. 2019, ApJL, 887, L30
Kumar, P., & Zhang, B. 2014, PhR, 561, 1
Law, C. J., Butler, B. J., Prochaska, J. X., et al. 2020, ApJ, 899, 161
Law, C. J., Sharma, K., Ravi., V., et al. 2024, ApJ, 967, 29
Li, D., & Pan, Z. 2016, RaSc, 51, 1060
Li, L.-Y., Jia, J.-Y., Qiang, D.-C., & Wei, H. 2024, arXiv:2408.12983
Li, X. J., Dong, X. F., Zhang, Z. B., & Li, D. 2021, ApJ, 923, 230
Li, Z., Gao, H., Wei, J.-J., et al. 2019, ApJ, 876, 146
Lloyd, S. 1982, ITIT, 28, 129
Lorimer, D. R. 2018, NatAs, 2, 860
Lorimer, D. R., Bailes, M., McLaughlin, M. A., Narkevic, D. J., & Crawford, F. 2007, Sci, 318, 777
Luo, J.-W., Zhu-Ge, J.-M., & Zhang, B. 2022, MNRAS, 518, 1629
MacQueen, J., et al. 1967, in Proc. Fifth Berkeley Symposium on Mathematical Statistics and Probability, ed. L. M. Le Cam & J. Neyman (Berkeley, CA: University of California Press), 281
McGregor, K., & Lorimer, D. R. 2024, ApJ, 961, 10
McInnes, L., Healy, J., & Astels, S. 2017, JOSS, 2, 205
McInnes, L., Healy, J., & Melville, J. 2018, arXiv:1802.03426
Niu, C. H., Aggarwal, K., Li, D., et al. 2022, Natur, 606, 873
Petroff, E., Barr, E. D., Jameson, A., et al. 2016, PASA, 33, e045
Petroff, E., Hessels, J. W. T., & Lorimer, D. R. 2022, A&ARv, 30, 2
Petroff, E., Keane, E. F., Barr, E. D., et al. 2015, MNRAS, 451, 3933
Planck Collaboration, Aghanim, N., Akrami, Y., et al. 2020, A&A, 641, A6
Pleunis, Z., Good, D. C., Kaspi, V. M., et al. 2021, ApJ, 923, 1
Qiang, D.-C., Deng, H.-K., & Wei, H. 2020, CQGra, 37, 185022
Qiang, D.-C., Li, S.-L., & Wei, H. 2022, JCAP, 01, 040
Qiang, D.-C., & Wei, H. 2020, JCAP, 04, 023
Qiang, D.-C., & Wei, H. 2021, PhRvD, 103, 083536
Raquel, B. J. R., Hashimoto, T., Goto, T., et al. 2023, MNRAS, 524, 1668
Ravi, V. 2019, NatAs, 3, 928
Ravi, V., & Lasky, P. D. 2014, MNRAS, 441, 2433
Rousseeuw, P. J. 1987, JCoAM, 20, 53
Rumelhart, D. E., Hinton, G. E., & Williams, R. J. 1986, Natur, 323, 533
Shannon, R. M., Bannister, K. W., Bera, A., et al. 2024, arXiv:2408.02083
Sharma, K., Ravi, V., Connor, L., et al. 2024, Natur, 635, 61
Spitler, L. G., Cordes, J. M., Hessels, J. W. T., et al. 2014, ApJ, 790, 101
Spitler, L. G., Scholz, P., Hessels, J. W. T., et al. 2016, Natur, 531, 202
Sun, W.-P., Zhang, J.-G., Li, Y., et al. 2025, ApJ, 980, 185
Thornton, D., Stappers, B., Bailes, M., et al. 2013, Sci, 341, 53
Vapnik, V. 1999, ITNN, 10, 988
Wagstaff, K. L., Tang, B., Thompson, D. R., et al. 2016, PASP, 128, 084503
Wang, B., & Wei, J.-J. 2023, ApJ, 944, 50
Wang, F. Y., Wang, Y. Y., Yang, Y.-P., et al. 2020a, ApJ., 891, 72
Wang, F. Y., & Zhang, G. Q. 2019, ApJ, 882, 108
Wang, W.-Y., Xu, R., & Chen, X. 2020b, ApJ, 899, 109
Wei, J.-J., Li, Z., Gao, H., & Wu, X.-F. 2019, JCAP, 09, 039
Wu, D., Cao, H., Lv, N., et al. 2019, ApJL, 887, L10
Xiao, D., & Dai, Z.-G. 2022, A&A, 657, L7
Xiao, D., Wang, F., & Dai, Z. 2021, SCPMA, 64, 249501
Xiao, D., Wang, F., & Dai, Z. 2022, in Fast Radio Bursts, ed. C. Bambi & A. Santangelo (Singapore: Springer), 1
Xu, H., Niu, J. R., Chen, P., et al. 2022, Natur, 609, 685
Xu, J., Feng, Y., Li, D., et al. 2023, Univ, 9, 330
Yamasaki, S., Goto, T., Ling, C.-T., & Hashimoto, T. 2023, MNRAS, 527, 11158
Yang, X., Zhang, S. B., Wang, J. S., & Wu, X. F. 2023, MNRAS, 522, 4342
Yang, X., Zhang, S. B., Wang, J. S., et al. 2021, MNRAS, 507, 3238
Yang, Y.-P., Luo, R., Li, Z., & Zhang, B. 2017, ApJL, 839, L25
Yang, Y.-P., & Zhang, B. 2016, ApJL, 830, L31
Zhang, B. 2014, ApJL, 780, L21
Zhang, B., Zhang, B.-B., Liang, E.-W., et al. 2007, ApJL, 655, L25
Zhang, M.-J., & Li, H. 2018, EPJC, 78, 460
Zhang, R. C., & Zhang, B. 2022, ApJL, 924, L14
Zhang, R. C., Zhang, B., Li, Y., & Lorimer, D. R. 2021, MNRAS, 501, 157
Zhang, Y. G., Gajjar, V., Foster, G., et al. 2018, ApJ, 866, 149
Zhou, B., Li, X., Wang, T., Fan, Y.-Z., & Wei, D.-M. 2014, PhRvD, 89, 107303
Zhu-Ge, J.-M., Luo, J.-W., & Zhang, B. 2022, MNRAS, 519, 1823
Zhu-Ge, J.-M., Luo, J.-W., & Zhang, B. 2023, MNRAS, 519, 1823